

Epidemic Management and Control Through Risk-Dependent Individual Contact Interventions

Tapio Schneider,* Oliver R. A. Dunbar,* Jinlong Wu, Dmitry Burov, and Chiara Daraio

California Institute of Technology, Pasadena, CA

Lucas Böttcher

*Computational Social Science, Frankfurt School of
Finance and Management, Frankfurt a. M., Germany[†]*

Alfredo Garbuno-Iñigo

*Departamento de Estadística, Instituto Tecnológico
Autónomo de México, Ciudad de México, México*

Gregory L. Wagner and Raffaele Ferrari

Massachusetts Institute of Technology, Cambridge, MA

Sen Pei and Jeffrey Shaman

Department of Environmental Health Sciences, Mailman School of Public Health

(Dated: September 24, 2021)

Abstract

Abstract: Testing, contact tracing, and isolation (TTI) is an epidemic management and control approach that is difficult to implement at scale. Here we demonstrate a scalable improvement to TTI that uses data assimilation (DA) on a contact network to learn about individual risks of infection. Network DA exploits diverse sources of health data together with proximity data from mobile devices. In simulations of the early COVID-19 epidemic in New York City, network DA identifies up to a factor 2 more infections than contact tracing when harnessing the same diagnostic test data. Targeting contact interventions with network DA reduces deaths by up to a factor 4 relative to TTI, provided compliance reaches around 75%. Network DA can be implemented by expanding the backend of existing exposure notification apps, thus greatly enhancing their capabilities. Implemented at scale, it has the potential to precisely and effectively control the ongoing or future epidemics while minimizing economic disruption.

Popular Summary: During the ongoing COVID-19 pandemic, exposure notification apps have been developed to scale manual contact tracing to larger groups of users. The apps use proximity data from mobile devices to automate finding and notifying direct contacts of an infection source. They suffer from lack of trust as they provide users only with rare and binary alerts. Here we present network data assimilation (DA) as a new digital approach to epidemic management and control. Network DA uses the same data as exposure notification apps but does so much more effectively and provides frequently updated individual risk assessments to users.

Network DA is based on automated learning about individuals' risk of infectiousness from crowd-sourced health data and proximity data. The data are aggregated with models of disease transmission and progression to produce statistical assessments of users' risks. In an extensive simulation study of the COVID-19 epidemic in New York City (NYC), we show that network DA with regular diagnostic testing could have achieved epidemic control with fewer than half the deaths that actually occurred during NYC's lockdown, all while typically having only 5–10% of the population in isolation at any given time.

Implemented at scale, network DA thus has the potential to effectively control the ongoing or future epidemics while minimizing the economic and social disruption of lockdowns.

* Joint first author

† Also at Department of Computational Medicine, University of California, Los Angeles, CA

I. INTRODUCTION

Until a majority of the global population has reached immunity against continuously evolving virus variants through vaccination or infection, the ongoing COVID-19 pandemic, as well as future pandemics, will need to be fought with non-pharmaceutical interventions (NPIs). They include social distancing, mask usage, and restrictions of mass gatherings. But NPIs such as lockdowns come at catastrophic costs to individuals, economies, and societies, with disproportionate burdens carried by disadvantaged groups [14, 29]. Even if imposed only intermittently and regionally, lockdowns are an inefficient means of epidemic management and control: they isolate much of the population, although even at extreme epidemic peaks, only a small fraction is infectious [28, 42]. If individuals who are at high risk of being infectious could be identified before they infect others, control measures could be made more efficient by targeting them to this high-risk group.

Testing and contact tracing have been discussed and partly implemented as strategies to identify individuals who are at high risk of being infectious [19, 23, 30]: testing determines who is infectious, contact tracing identifies those who may have been exposed through contact with an infectious individual, and this high-risk group is then isolated. However, controlling the COVID-19 epidemic by testing, contact tracing, and isolation (TTI) has been complicated by frequent asymptomatic and presymptomatic transmission, which support silent spread, and a short serial interval, the period between the onset of any symptoms in infector and infectee [22, 23, 33, 40]. Even in ideal scenarios, contact tracing needs to identify upward of 75% of infections to achieve epidemic control [19, 40]. Quickly diagnosing such a large fraction of infections and manually identifying exposed individuals requires testing and a contact tracing workforce at a scale that has been challenging to realize in most countries [2, 59].

To scale up contact tracing without a massive expansion of the workforce, exposure notification apps have been developed. They rely on proximity data from smartphones or other mobile devices to identify close contacts between users [6, 12]. If an individual user is identified as being infectious, prior close contacts are notified and can then self-isolate. The exposure notification is deterministic (a user is only notified when potentially exposed), and it only uses nearest-neighbor information on the network of close contacts among users. Exposure notification apps have not seen widespread use, in part perhaps because of early

implementation difficulties and privacy concerns but likely also because they do not provide users with information except in the rare case when they receive an exposure notification [32]. Nonetheless, where they have been used, these apps have helped prevent spread of infections [61].

Here we present a new and much more effective way of exploiting the same information on which exposure notification apps rely. Unlike these apps, however, this method provides users with continuously updated information about their individual risks. The core idea is to learn about individual risks of exposure and infectiousness by propagating crowdsourced information about infection risks over a dynamic contact network assembled from proximity data from mobile devices. Instead of the deterministic assessments of exposure notification apps, our approach exploits data from diverse sources probabilistically. Various types of information, including their uncertainties, can be harnessed. For example:

- Diagnostic tests, including sensitive but slow molecular tests, less sensitive but rapid antigen tests, or pooled diagnostic tests [53].
- Serological tests, which indicate a reduced probability of susceptibility when antibodies specific to SARS-CoV-2 (or the causative agent of another targeted disease) are detected.
- Self-reported clinical symptoms, elevated body temperature readings, or other wearable sensor data, which can indicate an elevated probability of infectiousness and virus transmission [10, 44].

Quantification of individual risks is achieved by assimilating data into a model of virus transmission and disease progression defined on the dynamic contact network. For decision making, periodically updated individual risks of having been exposed or of being infectious take the place of the deterministic assessments in exposure notification apps. The probabilistic network approach propagates data farther along the contact network than contact tracing. It harnesses more information than contact tracing, both by being able to include diverse data sources with their uncertainties and by exploiting information inherent in the network structure itself: an individual with many contacts generally is at greater risk of having been exposed than an individual with fewer contacts [35, 39].

The network and the information it contains are dynamically updated in periodic data assimilation (DA) cycles. These cycles resemble the daily DA cycles that weather forecasting

centers use operationally [8]. The quantitative information that is provided by the risk assessment platform we outline in what follows can be used in similar ways as weather forecasts: to inform personal decisions by users based on their desire to avoid risk (in the weather forecasting analogy, staying home rather than going on a mountain in the face of a likely downpour) and to inform public policy when aggregate risk measures indicate that wider mandates are necessary (analogous to evacuating a city to protect lives and avoid overwhelming public health and social infrastructures when a hurricane is likely to make landfall).

II. NETWORK DATA ASSIMILATION

Our point of departure is a variant of the widely used susceptible–exposed–infectious–resistant (or recovered) (SEIR) model of epidemiology, extended through inclusion of hospitalized (H) and deceased (D) compartments to an SEIHRD model [7]. While compartmental epidemiological models have traditionally been applied on the level of aggregated individuals (e.g., the population of a city or country) [9], here we apply the SEIHRD on an individual level on a time-dependent contact network [27, 39]. Each individual is represented by a node on the network; time-dependent edges between the nodes are established by close contacts between individuals, as recorded by proximity data from mobile devices. Virus transmission can occur during close contacts from infectious or hospitalized nodes to susceptible nodes, which thereupon become exposed. The probability of transmission increases with contact duration, and the transmission rate can vary from node to node and with time, for example, to reflect time-varying transmission rates resulting from virus mutations or a reduced transmission rate when masks are worn. From being exposed, nodes progress to becoming infectious, and later they may progress to requiring hospitalization, recover, or die.

At any time t , each node i is in one of the six health and vital states $S_i(t)$, $E_i(t)$ etc. of the SEIHRD model (see Methods). Network DA learns about the probabilities $\langle S_i(t) \rangle$, $\langle E_i(t) \rangle$, etc. of finding an individual node i at time t in each of the different states. We adopt a sequential Bayesian learning approach that propagates an ensemble of individual probabilities $\langle S_i(t) \rangle$, $\langle E_i(t) \rangle$, etc. across the network and periodically updates them and the SEIHRD model parameters with new data [4, 33, 41, 51]. Data falling within a DA window of length Δ (typically $\Delta \approx 1$ day) are incorporated into the model by adjusting the ensemble to

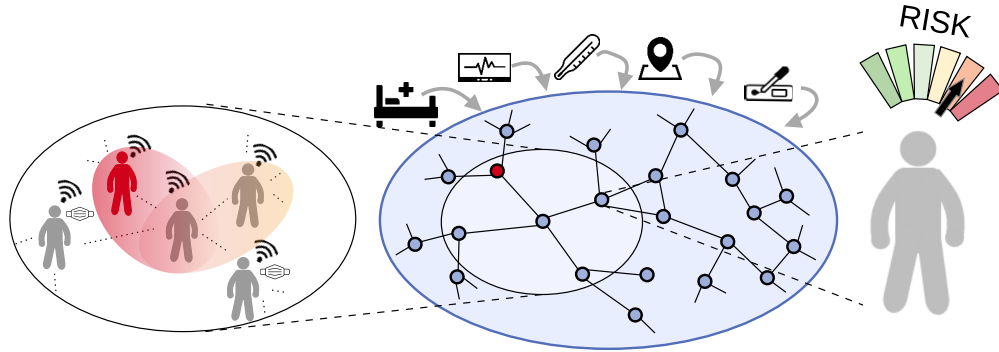


FIG. 1. Schematic of the personalized risk assessment platform. Proximity-tracking data from mobile devices is used to assemble a contact network, in which nodes represent individuals, and edges represent close contacts between individuals. An epidemiological model defined on the contact network is then fused with diverse health data, including diagnostic tests, hospitalization status, and possibly data such as body temperature readings. The model spreads risk of infectiousness from a positive individual (red) to others, taking into account knowledge about disease progression, the time and duration of contacts, and the use of personal protective equipment (PPE), among other factors. The result of the network DA is an assessment of individual risks, for example, of being infectious, which then can be used to target contact interventions.

minimize the misfit to the data in the window. An interval Δ later, the updating procedure is repeated (see Methods for details). Such DA cycles and the underlying algorithms are used daily in weather forecasting to estimate up to 10^9 variables characterizing the state of the atmosphere; they easily scale to network epidemiology models with millions of nodes or more. Essentially all types of data and their error characteristics can be assimilated with this approach, even data that are less sensitive to infectiousness, such as readings of heart rates [45] or body temperatures [10, 44] (Fig. 1).

III. SYNTHETIC NETWORK FOR PROOF-OF-CONCEPT

To demonstrate the methods, we construct a large synthetic contact network with $N = 97,942$ nodes and about 1 million connections among them. The network has typical characteristics of a human contact network. It has a time-dependent contact rate minimum at night and a maximum midday, and it has a connectivity (degree) distribution similar to human networks: there are many individuals with few connections and a few highly con-

nected individuals who are more likely to become superspreaders [16] (Fig. S5). The network also contains a block representing hospitals, where hospitalized patients are connected to healthcare workers, who in turn are connected to the community in the rest of the network. However, the present network omits some features of human contact networks, such as household, workplace, and school structures.

As surrogates for the real world, we use stochastic simulations of the epidemiology model for the state variables $S_i(t)$, $E_i(t)$, etc. on the network. To obtain simulations resembling the real world, we randomly assign ages to nodes according to the age distribution of New York City (NYC), and we use those ages to model age-dependent disease progression according to current knowledge about COVID-19 (Tables II and III). With these surrogate worlds, we explore how individual risk assessment and epidemic management and control can be achieved in what-if scenarios.

IV. RESULTS

A. Lockdown and world avoided

As an illustrative example, we simulate the evolution of an epidemic that, when scaled up from our network size to the NYC population of 8.3 million, resembles the early evolution of the COVID-19 epidemic in NYC in 2020 (Fig. 2). If the contact rate on the network remains unchanged in the simulations, the number of infections and deaths rises from early March into April, with daily deaths reaching a peak of around 21 per 100,000 population in the second half of April.

However, this world was avoided by a lockdown, which became mandatory in NYC from March 22 onward. In its wake, the number of daily new cases and deaths began to decline from mid-April onward (Fig. 2). We can reproduce similar behavior in the stochastic simulations by reducing the average contact rate of all nodes by 58% starting March 25 (Fig. 2). The infection rates in the stochastic simulations exceed the number of confirmed cases in NYC because the latter undercount actual infections [62]. However, the death rates in the stochastic simulations are close to the NYC death rate (Fig. 2), and so are the hospitalization rates (Fig. S7).

The similarity of the synthetic and observed epidemics shows that the synthetic epidemics

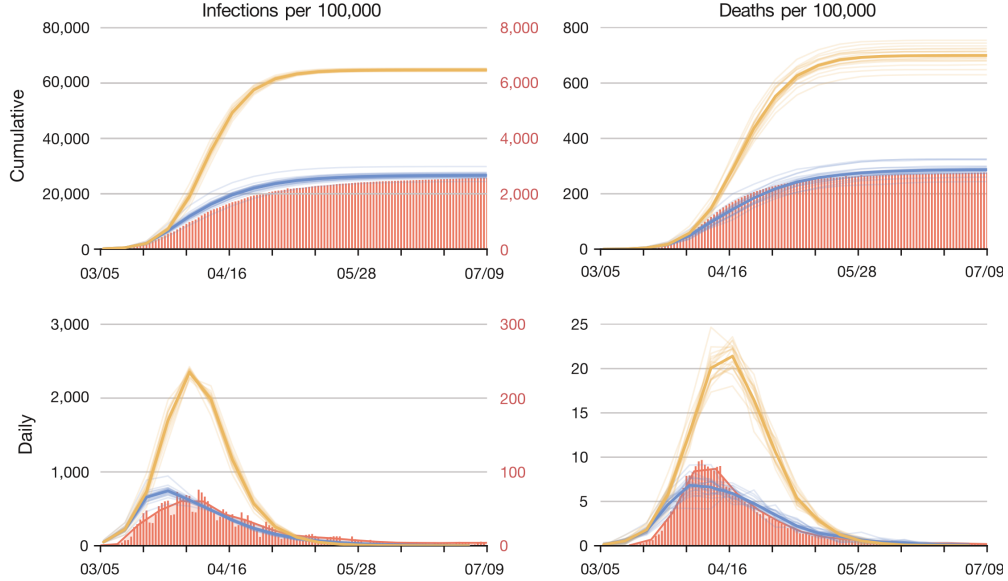


FIG. 2. Evolution of an outbreak in surrogate-world simulations with a lockdown (blue) and without (orange). The left column shows infection rates and the right column death rates. Upper row for cumulative counts and lower row for daily counts, smoothed with a 7-day moving average filter. Red bars represent confirmed and probable COVID-19 deaths and confirmed infection rates for New York City [1], with the red axis labels on the right for confirmed infection counts. Solid lines indicate the corresponding counts in the simulations, with the black axis labels on the left for infections on the network. (The axes for infections in the simulations are stretched by a factor 10 relative to the axes for confirmed NYC infections, reflecting the undercount of total infections by confirmed cases [62].) The light lines show 20 simulations that only differ by random seeds, with the thicker lines indicating the ensemble mean. The average contact rate for all nodes is reduced by 58% from March 25, 2020 onward to mimic the lockdown effect (blue solid line).

can be used to illustrate the concepts of the risk assessment platform we envisage.

B. Accuracy of individual risk assessment

To demonstrate the accuracy of individual risk assessments, we assume the network DA platform has $\tilde{N} \leq N$ users who exchange proximity data with each other, with 25% to 100% of the population in the user base (i.e., $0.25 \leq \tilde{N}/N \leq 1$). For subsets of the \tilde{N} users, we assimilate results of simulated rapid diagnostic tests from the corresponding nodes in the

surrogate-world simulation. A fraction $f = 5\%$, 10% , or 25% of the user base is assumed to be tested daily, with results available on the day of test administration; that is, every user is tested on average every 20, 10, or 4 days (Methods).

We first illustrate network DA in the worst-case scenario of the free-running synthetic epidemic, in which contact patterns do not change. DA begins on March 5. We show results for April 9, near the epidemic peak, when about 7% of the population are infectious, and for April 30, when new infections are waning (Fig. 2). (In this free-running epidemic, the maximum prevalence of infectiousness is considerably higher than in the lockdown simulations, in which prevalence peaks at 1.5%–2%.)

We classify users i as possibly infectious (“positive”) when the estimated probability of infectiousness $\langle I_i(t) \rangle$ exceeds a threshold c_I . The true positive rate (TPR) at which users are correctly classified as positive (i.e., they are indeed infectious in the stochastic surrogate-world simulation) increases as the classification threshold c_I decreases; at the same time, the positive predicted fraction (PPF)—the rate at which users overall are classified as positive, whether correctly or incorrectly—also increases because the false positive rate (FPR) increases. Receiver operating curves (ROC) trace out these competing changes in TPR and PPF (or FPR) as the classification threshold c_I is varied (Fig. 3). Choosing a classification threshold c_I means finding a trade-off between wanting a high TPR while keeping PPF and FPR low. In the ideal albeit unrealistic scenario when the user base encompasses the whole population ($\tilde{N}/N = 100\%$), TPRs for April 9 range from 19% to 47% for a PPF of 8% and test rates from $f = 5\%$ to 25% ; for April 30, TPRs range from 27% to 59% (Fig. 3a, b). That is, the classification results improve as the network model learns about the evolution of the epidemic. The classification results are insensitive to the user base coverage \tilde{N}/N (Fig. 3c, d), as well as to the user base topology; for example, classification performance is not substantially affected whether the user base consists of neighborhoods in the total population network (Fig. 3) or of random nodes (Fig. S8).

To put these results in context, consider the following two traditional approaches:

- If only users with positive diagnostic tests are classified as positive, TPRs reach 4%, 9%, and 22% for test rates $f = 5\%$, 10% , and 25% , respectively, with PPFs below 1.8% on April 9 and below 0.6% on April 30 (Fig. 3a, b, solid circles). This test-only TPR is close to but slightly smaller than f because the test sensitivity is less than 100%. Classification by network DA can achieve substantially higher TPRs than

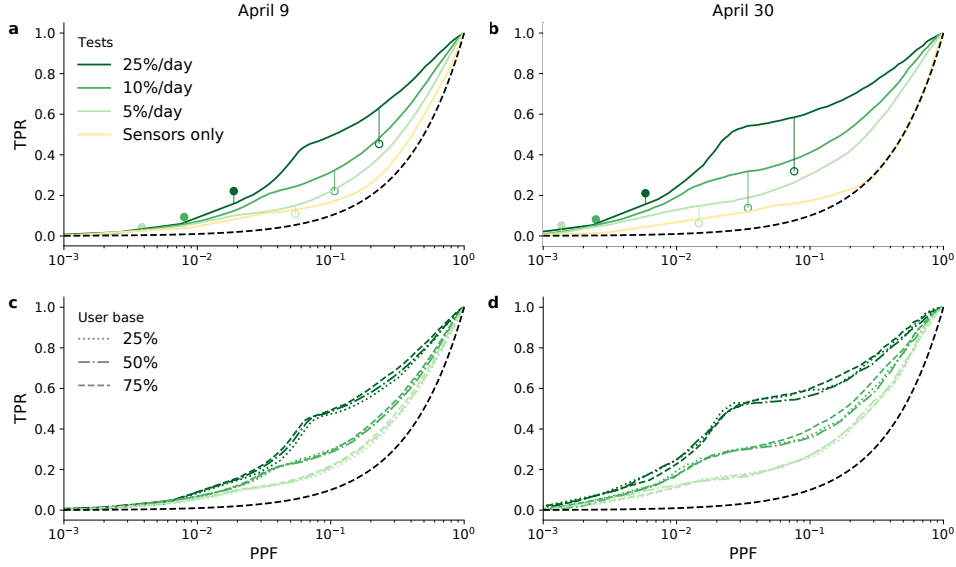


FIG. 3. Receiver operating characteristic (ROC) curves for classification as possibly infectious. ROC curves trace out the true positive rate (TPR) vs the predicted positive fraction (PPF) as the classification threshold is varied. TPR and PPF are given relative to the user base size \tilde{N} . Green shades of the ROC curves from lighter to darker correspond to increasing diagnostic test rates f . Left column for April 9; right column for April 30. (a, b) For the ideal user base of $\tilde{N}/N = 100\%$. For comparison, the filled circles are for a test-only scenario when only users with positive diagnostic tests are classified as positive; the open circles are for a contact-tracing scenario in which additionally prior close contacts of users with positive diagnostic tests are classified as positive. Also shown is a sensors-only scenario in which 75% of the user base is assumed to provide daily body temperature readings. (c, d) For user bases of 25%, 50%, and 75%, with the same test rates f in shades of green as in (a, b). The black dashed line represents a random classifier.

testing alone, at the expense of increased but still modest PPFs.

- Contact tracing and exposure notification apps classify as positive users with positive diagnostic tests, plus their potentially exposed nearest neighbors on the network. If individuals are classified as positive if, over the 10 days preceding the diagnosis, they had at least one contact of more than 15 minutes length with a user who had a positive diagnostic test, the contact-tracing TPRs range from 11% to 45% for test rates from $f = 5\%$ to 25%, with PPFs between 5% and 23% (Fig. 3a, b, open circles). Network

DA exploits the same data as contact tracing but achieves substantially higher TPRs at the same PPF. For example, at the contact-tracing PPF, network DA achieves about a 40% higher TPR than contact tracing for April 9, and about a factor 2 higher TPR for April 30 (Fig. 3a, b, vertical lines above open circles).

Network DA can also be used to assess quantitatively to what extent lower-fidelity data can improve classification. As an example, we conducted a set of experiments in which 75% of the users were assumed to report body temperatures daily—for example, with wearable sensors [44]—with infectiousness indicated by elevated temperature readings with 20% sensitivity [10]. Such temperature readings improve the classification when no or very few diagnostic tests are available, but they do not provide a substantial benefit when $f = 5\%$ of the user base or more can be tested daily (Fig. 3a, b). Nonetheless, if widely adopted, temperature sensors can provide a modest benefit when diagnostic testing capacity is low [44].

The results show that network DA allows identification of a large fraction of infectious individuals, provided widespread testing is available. For a sufficiently large user base coverage \tilde{N}/N , this capability can be used to tailor individualized contact interventions for epidemic management and control.

C. Risk-tailored contact interventions

The individual risk assessments can be used to prompt those who are classified as possibly infectious for contact interventions. As an illustrative example of such individual contact interventions, we assume that users of the app self-isolate by reducing their contact rate with others by 91%, to an average of 4 contacts per day, during the time when they are classified as positive and 5 subsequent days; all others in the population, whether app users or not, do not change their behavior. For comparison, we present TTI scenarios with the same contact rate reduction but continuing over 14 days after diagnosis or identification as possibly exposed through contact with an infectious individual; for a direct comparison with the network DA, TTI compliance is assumed to be confined to the user base. We focus the presentation on the end-member testing regimes with test rates $f = 5\%$ and 25% . As classification threshold, we choose $c_I = 1\%$, resulting in $\text{TPR} \gtrsim 40\%$ and $\text{PPF} \lesssim 9\%$ when contact interventions commence.

In the idealized case with full user base coverage ($\tilde{N}/N = 100\%$), the epidemic is more strongly suppressed with the network DA interventions than in the lockdown scenario, with 50–70% fewer cumulative deaths (Fig. 4). However, whereas in the lockdown scenario the entire population has reduced contacts, with network DA only a small fraction of the population self-isolates. The self-isolation fraction has an initial peak of 15–17% for about a week and then falls quickly to 5–10%, with damped relaxation oscillations over several weeks in the case with lower test rates ($f = 5\%$); 50% of those who isolate do so for 7 days or less, and 90% for 14 days or less. That is, in this idealized case, risk-tailored self-isolation achieves effective epidemic control with isolation of only a small fraction of the population at a time. For comparison, TTI with 100% compliance also achieves epidemic control; however, at the test rate $f = 5\%$, cumulative deaths are 3 times higher than with network DA because TTI misses more infections than network DA. At the test rate $f = 25\%$, the cumulative death rate with TTI is comparable to or lower than with network DA, but at the expense of a 2–5 times higher isolated fraction of the population. Whereas the performance of TTI is strongly test-rate dependent, that of network DA is less sensitive to test rate, and it is always more efficient to TTI.

In the more realistic case with $\tilde{N}/N = 75\%$ user base coverage, risk-tailored self-isolation still achieves epidemic control at both test rates (Fig. 5), with a cumulative death rate similar to the 100% user base. The fraction of the population in isolation again peaks at just over 15% initially and then drops to 5–10%. As before, TTI with 75% compliance and with the higher test rate ($f = 25\%$) also achieves epidemic control, but with a higher isolated fraction of the population; at the lower test rate ($f = 5\%$), TTI results in an about four times higher cumulative death rate than isolation tailored by network DA, which additionally isolates fewer individuals.

With a user base coverage of $\tilde{N}/N = 50\%$, classification remains accurate and isolation tailored by network DA can still achieve epidemic control and can remain more effective than a lockdown in preventing infections and deaths (Fig. S10). The initial fraction of the population in isolation increases to around 30%, and then drops again to between 5–10%. However, this means that initially, the majority of the user base (50% of population) is in isolation, which, in a case of perverse incentives, effectively puts the user base, but not others, in a lockdown. TTI with 50% compliance fails to control the epidemic for $f = 5\%$ but still achieves control at $f = 25\%$, albeit with a higher isolated population fraction than

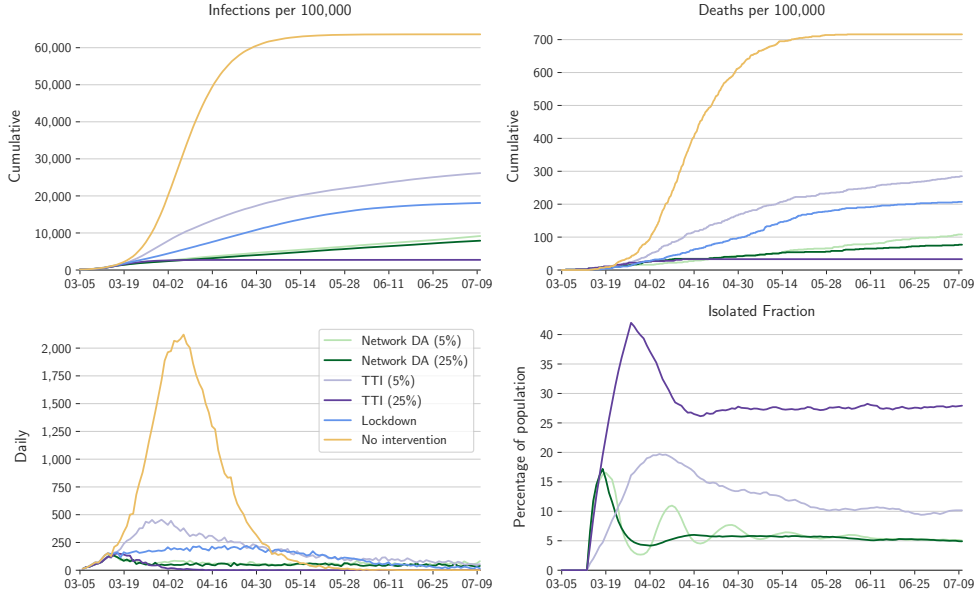


FIG. 4. Comparison of different contact intervention scenarios for full user base with $\tilde{N}/N = 100\%$. Shown are the free-running epidemic without interventions (orange) and the lockdown scenario (blue) from Fig. 2, the results of network DA and isolation of positive individuals for test rates $f = 5\%$ and 25% (greens), and the results of TTI with the same test rates as for network DA (purples).

with network DA.

These results for reduced user bases are for sub-networks consisting of neighborhoods in the overall population network. Results for user bases consisting of nodes selected at random from the overall population are qualitatively similar for $\tilde{N}/N = 75\%$, albeit with an adjusted classification threshold and a higher fraction of the population in isolation (Figs. S9). For $\tilde{N}/N = 50\%$ with a random user base, network DA, while still being able to identify a large fraction of infectious individuals in the user base (Fig. S8), ceases to be effective for epidemic control (Fig. S11); however, it is possible its performance may be improved with data-adaptive classification thresholds.

V. DISCUSSION

We have demonstrated the concept of a platform for individual health risk assessment, which exploits the same proximity data from mobile devices that exposure notification apps

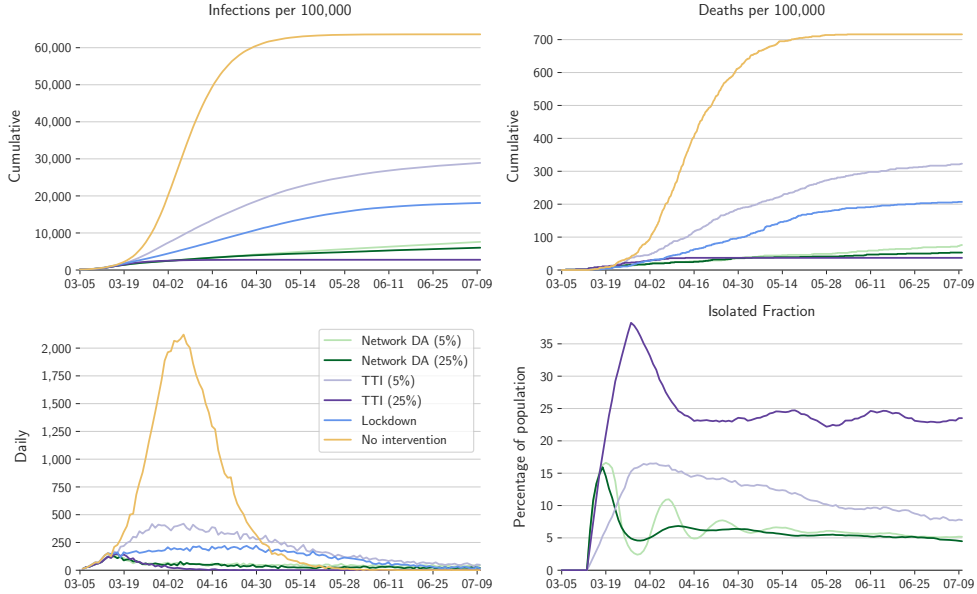


FIG. 5. Comparison of different contact intervention scenarios for a user base with $\tilde{N}/N = 75\%$. Plotting conventions as in Fig. 4. TTI here is confined to the same user base as network DA, implying 75% compliance.

rely upon but is substantially better at identifying infectious individuals. It achieves these gains by assimilating crowdsourced data from diverse sources into an epidemiological model defined on a contact network. Network DA provides informative and actionable risk assessments for individuals, even when only a modest fraction of the population uses the app necessary to obtain proximity data. When the user base is sufficiently large (covering around 75% of the population), the platform can be used to tailor interventions that are more efficient for epidemic management and control than lockdowns or TTI. For example, with a user base covering 75% of the population and users tested every 20 days, simulations for NYC showed that risk-tailored self-isolation achieves epidemic control with 63% fewer deaths than during NYC’s lockdown, with typically only 5–10% of the population in isolation at any given time. This risk-tailored isolation approach is also more effective in preventing infections and deaths than TTI that uses the same network and diagnostic testing data.

The platform can be realized with existing technology by expanding the backend of exposure notification apps. High-precision proximity data are now available through Bluetooth protocols [6], and lower-precision location data from mobile devices have been exploited commercially for some time. To be effective, the platform requires that users opt-in to pro-

vide proximity data and other crowdsourced data, such as test results and reports of clinical symptoms. The more detailed data users make available, the more accurate and detailed risk profiles can be produced in return.

The data would have to be transferred temporarily to a central computing facility for data assimilation, posing challenges in protecting users' privacy. Because of the central processing requirement, it is somewhat more difficult to harden the platform against malicious exploitation than it is for exposure notification apps, which only require central data exchange when there is direct evidence of an infection [24]. Nonetheless, the data need not be stored beyond a data assimilation window that is at most a few days long. Additionally, the platform requires only anonymized proximity data but not absolute location data, and it does not rely on humans in the loop, reducing risks of malicious exploitation. There may be ways to harden the platform itself and the data exchange with users against privacy breaches [57].

The network DA platform provides obvious benefits in managing and controlling epidemics, for example, in reducing the need for lockdowns while preventing infections and deaths, and in providing users tools to manage their personal risks. It provides a scalable and more accurate alternative to the digital or manual TTI programs developed by many governments, including that of NYC [37]. The effectiveness of such programs has been modelled [19, 23, 30], but their impact in practice is only beginning to be elucidated [61]. Given that many TTI programs are voluntary, and documentation of contacts is subjective, it will be important to compare both the control and cost effectiveness of manual trace programs with the more objective and automated network DA approach presented here.

In addition to its health impacts, the COVID-19 pandemic has exacted an enormous economic toll on countries throughout the world [14, 29]. There is a continuing need to identify approaches that precisely and effectively control epidemics while minimizing economic disruption. With sufficient uptake and testing, the platform described here provides a means for achieving these dual aims.

ACKNOWLEDGMENTS

We thank Tobias Bischoff, Mason Porter, and Andrew Stuart for helpful discussions. This research was supported by Eric and Wendy Schmidt and Schmidt Futures (T.S., O.R.A.D.,

J.W., D.B.); Swiss National Science Foundation (P2EZP2_191888), National Institutes of Health (R01HL146552), and Army Research Office (W911NF-18-1-0345) (L.B.); National Science Foundation (DMS-2027369) (S.P., J.S.) and the Morris-Singer Foundation (J.S.).

- [1] *NYC Coronavirus Disease 2019 (COVID-19) Data*. <https://github.com/nychealth/coronavirus-data>, 2020.
- [2] D. ALLEN, S. BLOCK, J. COHEN, P. ECKERSLEY, M. EIFLER, L. GOSTIN, D. GOUX, D. GRUENER, V. HART, Z. HITZIG, J. KLEIN, J. LANGFORD, T. NORDHAUS, M. ROSENTHAL, R. SETHI, ET AL., *Roadmap to pandemic resilience: Massive scale testing, tracing, and supported isolation (TTSI) as the path to pandemic resilience for a free society*, tech. rep., Edmond J. Safra Center for Ethics at Harvard University, April 20 2020.
- [3] F. ALTARELLI, A. BRAUNSTEIN, L. DALL’ASTA, A. LAGE-CASTELLANOS, AND R. ZECCHINA, *Bayesian inference of epidemics on networks via belief propagation*, *Phys. Rev. Lett.*, 112 (2014).
- [4] J. L. ANDERSON, *An ensemble adjustment Kalman filter for data assimilation*, *Mon. Wea. Rev.*, 129 (2001), pp. 2884–2903.
- [5] ———, *Localization and sampling error correction in ensemble Kalman filter data assimilation*, *Mon. Wea. Rev.*, 140 (2012), pp. 2359–2371.
- [6] APPLE/GOOGLE, *Privacy-preserving contact tracing*, 2020. <https://www.apple.com/covid19/contacttracing>.
- [7] A. ARENAS, W. COTA, J. GÓMEZ-GARDEÑES, S. GÓMEZ, C. GRANELL, J. T. MATAMALAS, D. SORIANO-PAÑOS, AND B. STEINEGGER, *Modeling the spatiotemporal epidemic spreading of COVID-19 and the impact of mobility and social distancing interventions*, *Phys. Rev. X*, 10 (2020), p. 041055.
- [8] P. BAUER, A. THORPE, AND G. BRUNET, *The quiet revolution of numerical weather prediction*, *Nature*, 525 (2015), pp. 47–55.
- [9] A. L. BERTOZZI, E. FRANCO, G. MOHLER, M. B. SHORT, AND D. SLEDGE, *The challenges of modeling and forecasting the spread of COVID-19*, *Proc. Natl. Acad. Sci.*, (2020).
- [10] M. BIELECKI, G. A. G. CRAMERI, P. SCHLAGENHAUF, T. W. BUEHRER, AND J. W. DEUEL, *Body temperature screening to identify SARS-CoV-2 infected young adult travellers*

- is ineffective*, *Travel Med. Infect. Dis.*, 37 (2020), p. 101832.
- [11] C. BROWN, A. NOULAS, C. MASCOLO, AND V. BLONDEL, *A place-focused model for social networks in cities*, in 2013 International Conference on Social Computing, IEEE, 2013, pp. 75–80.
- [12] G. CENCETTI, G. SANTIN, A. LONGA, E. PIGANI, A. BARRAT, C. CATTUTO, S. LEHMANN, M. SALATHÉ, AND B. LEPRI, *Digital proximity tracing on empirical contact networks for pandemic control*, *Nature Comm.*, 12 (2021), p. 1655.
- [13] CENTERS FOR DISEASE CONTROL AND PREVENTION, *Contact tracing for COVID-19*. <https://www.cdc.gov/coronavirus/2019-ncov/php/contact-tracing/contact-tracing-plan/contact-tracing.html>, 2021.
- [14] S. CHANG, E. PIERSON, P. W. KOH, J. GERARDIN, B. REDBIRD, D. GRUSKY, AND J. LESKOVEC, *Mobility network models of COVID-19 explain inequities and inform reopening*, *Nature*, 589 (2021), pp. 82–87.
- [15] A. DUVAL, T. OBADIA, L. MARTINET, P.-Y. BOËLLE, E. FLEURY, D. GUILLEMOT, L. OPATOWSKI, AND L. TEMIME, *Measuring dynamic social contacts in a rehabilitation hospital: effect of wards, patient and staff characteristics*, *Sci. Rep.*, 8 (2018), pp. 1–11.
- [16] A. ENDO, Q. J. LECLERC, G. M. KNIGHT, G. F. MEDLEY, K. E. ATKINS, S. FUNK, AND A. J. KUCHARSKI, *Implication of backward contact tracing in the presence of overdispersed transmission in COVID-19 outbreaks*, *Wellcome Open Res.*, 5 (2021), p. 239.
- [17] N. M. FERGUSON, D. A. CUMMINGS, S. CAUCHEMEZ, C. FRASER, S. RILEY, A. MEEYAI, S. IAMSIRITHAWORN, AND D. S. BURKE, *Strategies for containing an emerging influenza pandemic in Southeast Asia*, *Nature*, 437 (2005), pp. 209–214.
- [18] N. M. FERGUSON, D. A. T. CUMMINGS, C. FRASER, J. C. CAJKA, P. C. COOLEY, AND D. S. BURKE, *Strategies for mitigating an influenza pandemic*, *Nature*, 442 (2006), pp. 448–452.
- [19] L. FERRETTI, C. WYMANT, M. KENDALL, L. ZHAO, A. NURTAY, L. ABELER-DÖRNER, M. PARKER, D. BONSALE, AND C. FRASER, *Quantifying SARS-CoV-2 transmission suggests epidemic control with digital contact tracing*, *Science*, 368 (2020), p. eabb6936.
- [20] D. T. GILLESPIE, *Exact stochastic simulation of coupled chemical reactions*, *J. Phys. Chem.*, 81 (1977), pp. 2340–2361.

- [21] J. P. GLEESON, S. MELNIK, J. A. WARD, M. A. PORTER, AND P. J. MUCHA, *Accuracy of mean-field theory for dynamics on real-world networks*, Phys. Rev. E, 85 (2012), p. 026106.
- [22] X. HE, E. H. LAU, P. WU, X. DENG, J. WANG, X. HAO, Y. C. LAU, J. Y. WONG, Y. GUAN, X. TAN, ET AL., *Temporal dynamics in viral shedding and transmissibility of COVID-19*, Nature Medicine, 26 (2020), pp. 672–675.
- [23] J. HELLEWELL, S. ABBOTT, A. GIMMA, N. I. BOSSE, C. I. JARVIS, T. W. RUSSELL, J. D. MUNDAY, A. J. KUCHARSKI, W. J. EDMUNDS, F. SUN, ET AL., *Feasibility of controlling COVID-19 outbreaks by isolation of cases and contacts*, Lancet Global Health, 8 (2020), pp. E488–E496.
- [24] R. HINCH, W. PROBERT, A. NURTAY, M. KENDALL, C. WYMANT, M. HALL, K. LYTHGOE, A. B. CRUZ, L. ZHAO, A. STEWART, L. FERRETTI, M. PARKER, A. MEROUEH, B. MATHIAS, S. STEVENSON, D. MONTERO, J. WARREN, N. K. MATHER, A. FINKELSTEIN, L. ABELER-DÖRNER, D. BONSALE, AND C. FRASER, *Effective configurations of a digital contact tracing app: A report to NHSX*, tech. rep., April 2020.
- [25] P. L. HOUTEKAMER AND F. ZHANG, *Review of the ensemble Kalman filter for atmospheric data assimilation*, Mon. Wea. Rev., 144 (2016), pp. 4489–4532.
- [26] B. KARRER AND M. E. NEWMAN, *Stochastic block models and community structure in networks*, Phys. Rev. E, 83 (2011), p. 016107.
- [27] I. Z. KISS, J. C. MILLER, AND P. L. SIMON, *Mathematics of Epidemics on Networks*, Springer, 2017.
- [28] S. M. KISSLER, C. TEDIJANTO, E. GOLDSTEIN, Y. H. GRAD, AND M. LIPSITCH, *Projecting the transmission dynamics of SARS-CoV-2 through the postpandemic period*, Science, 368 (2020), pp. 860–868.
- [29] M. KÖNIG AND A. WINKLER, *COVID-19: Lockdowns, fatality rates and GDP growth*, Intereconomics, 56 (2021), pp. 32–39.
- [30] A. J. KUCHARSKI, P. KLEPAC, A. J. K. CONLAN, S. M. KISSLER, M. L. TANG, H. FRY, J. R. GOG, AND W. J. EDMUNDS, *Effectiveness of isolation, testing, contact tracing, and physical distancing on reducing transmission of SARS-CoV-2 in different settings: a mathematical modelling study*, Lancet Infect. Dis., 20 (2020), pp. P1151–1160.
- [31] S. A. LAUER, K. H. GRANTZ, Q. BI, F. K. JONES, Q. ZHENG, H. MEREDITH, A. S. AZMAN, N. G. REICH, AND J. LESSLER, *The incubation period of coronavirus disease 2019*

- (COVID-19) from publicly reported confirmed cases: Estimation and application, *Ann. Intern. Med.*, 172 (2020), pp. 577–582.
- [32] D. LEWIS, *Contact-tracing apps help reduce COVID infections, data suggest*, *Nature*, 591 (2021), pp. 18–19.
- [33] R. LI, S. PEI, B. CHEN, Y. SONG, T. ZHANG, W. YANG, AND J. SHAMAN, *Substantial undocumented infection facilitates the rapid dissemination of novel coronavirus (SARS-CoV2)*, *Science*, 368 (2020), pp. 489–493.
- [34] Q.-H. LIU, M. AJELLI, A. ALETA, S. MERLER, Y. MORENO, AND A. VESPIGNANI, *Measurability of the epidemic reproduction number in data-driven contact networks*, *Proc. Natl. Acad. Sci.*, 115 (2018), pp. 12680–12685.
- [35] L. A. MEYERS, B. POURBOHLOUL, M. E. NEWMAN, D. M. SKOWRONSKI, AND R. C. BRUNHAM, *Network theory and SARS: predicting outbreak diversity*, *J. Theor. Biol.*, 232 (2005), pp. 71–81.
- [36] J. MOSSONG, N. HENS, M. JIT, P. BEUTELS, K. AURANEN, R. MIKOLAJCZYK, M. MASSARI, S. SALMASO, G. S. TOMBA, J. WALLINGA, J. HEIJNE, ET AL., *Social contacts and mixing patterns relevant to the spread of infectious diseases*, *PLoS Medicine*, 5 (2008), p. e74.
- [37] NEW YORK CITY, *Test and trace corps*. <https://www1.nyc.gov/site/coronavirus/get-tested/test-trace-corps.page>, 2021.
- [38] M. E. NEWMAN, *Spread of epidemic disease on networks*, *Phys. Rev. E*, 66 (2002), p. 016128.
- [39] R. PASTOR-SATORRAS, C. CASTELLANO, P. V. MIEGHEM, AND A. VESPIGNANI, *Epidemic processes in complex networks*, *Rev. Mod. Phys.*, 87 (2015), pp. 925–979.
- [40] C. M. PEAK, R. KAHN, Y. H. GRAD, L. M. CHILDS, R. LI, M. LIPSITCH, AND C. O. BUCKEE, *Individual quarantine versus active monitoring of contacts for the mitigation of COVID-19: a modelling study*, *Lancet Infect. Dis.*, 20 (2020), pp. 1025–1033.
- [41] S. PEI, S. KANDULA, W. YANG, AND J. SHAMAN, *Forecasting the spatial transmission of influenza in the United States*, *Proc. Natl. Acad. Sci.*, 115 (2018), pp. 2752–2757.
- [42] S. PEI, S. KANDULAA, AND J. SHAMAN, *Differential effects of intervention timing on COVID-19 spread in the United States*, *Sci. Adv.*, 6 (2020), p. eabd6370.
- [43] T. P. PEIXOTO, *The graph-tool Python library*. doi:10.6084/m9.figshare.1164194, 2014.
- [44] G. QUER, J. M. RADIN, M. GADALETA, K. BACA-MOTES, L. ARINIELLO, E. RAMOS, V. KHETERPAL, E. J. TOPOL, AND S. R. STEINHUBL, *Wearable sensor data and self-reported*

- symptoms for COVID-19 detection*, Nature Medicine, 27 (2021), pp. 73–77.
- [45] J. M. RADIN, N. E. WINEINGER, E. J. TOPOL, AND S. R. STEINHUBL, *Harnessing wearable device data to improve state-level real-time surveillance of influenza-like illness in the USA: a population-based study*, Lancet Digital Health, 2 (2020), pp. e85–e93.
- [46] S. RICHARDSON, J. S. HIRSCH, M. NARASIMHAN, J. M. CRAWFORD, T. MCGINN, K. W. DAVIDSON, AND THE NORTHWELL COVID-19 RESEARCH CONSORTIUM, *Presenting characteristics, comorbidities, and outcomes among 5700 patients hospitalized with COVID-19 in the New York City area*, JAMA, 323 (2020), pp. 2052–2059.
- [47] E. S. ROSENBERG, J. M. TESORIERO, E. M. ROSENTHAL, R. CHUNG, M. A. BARRANCO, L. M. STYER, M. M. PARKER, S.-Y. J. LEUNG, J. MORNE, D. GREENE, ET AL., *Cumulative incidence and diagnosis of SARS-CoV-2 infection in New York*, Ann. Epidemiology, 48 (2020), pp. 23–29.
- [48] M. SALATHÉ, M. KAZANDJIEV, J. W. LEE, P. LEVIS, M. W. FELDMAN, AND J. H. JONES, *A high-resolution human contact network for infectious disease transmission*, Proc. Natl. Acad. Sci., 107 (2010), pp. 22020–22025.
- [49] H. SALJE, C. T. KIEM, N. LEFRANCQ, N. COURTEJOIE, P. BOSETTI, J. PAIREAU, A. ANDRONICO, N. HOZE, J. RICHEL, C.-L. DUBOST, ET AL., *Estimating the burden of SARS-CoV-2 in France*, Science, 368 (2020), p. eabc3517.
- [50] N. SETHURAMAN, S. S. JEREMIAH, AND A. RYO, *Interpreting diagnostic tests for SARS-CoV-2*, JAMA, 323 (2020), pp. 2249–2251.
- [51] J. SHAMAN AND A. KARSPECK, *Forecasting seasonal outbreaks of influenza*, Proc. Natl. Acad. Sci., 109 (2012), pp. 20425–20430.
- [52] K. J. SHARKEY, *Deterministic epidemiological models at the individual level*, J. Math. Biology, 57 (2008), pp. 311–331.
- [53] N. SHENTAL, S. LEVY, S. SKORNIKOV, V. WUVSHET, Y. SHEMER-AVNI, A. PORGADOR, AND T. HERTZ, *Efficient high-throughput SARS-CoV-2 testing to detect asymptomatic carriers*, Science Adv., 6 (2020), p. eabc5961.
- [54] SOCIOPATTERNS, *DATASET: High school dynamic contact networks*. <http://www.sociopatterns.org/publications/contact-patterns-among-high-school-students/>, 2014.

- [55] U.S. CENSUS, *Age demographics, New York, NY*. <https://datausa.io/profile/geo/new-york-ny#demographics>, 2018.
- [56] U.S. FOOD AND DRUG ADMINISTRATION, *EUA authorized serology test performance*. <https://www.fda.gov/medical-devices/emergency-situations-medical-devices/eua-authorized-serology-test-performance>, 2020.
- [57] M. B. VAN DER WAAL, C. DOS S. RIBEIRO, M. MA, G. B. HARINGHUIZEN, E. CLAASSEN, AND L. H. M. VAN DE BURG WAL, *Blockchain-facilitated sharing to advance outbreak R&D*, *Science*, 368 (2020), pp. 719–721.
- [58] W. WANG, Y. XU, R. GAO, R. LU, K. HAN, G. WU, AND W. TAN, *Detection of SARS-CoV-2 in different types of clinical specimens*, *JAMA*, 323 (2020), pp. 1843–1844.
- [59] C. WATSON, A. CICERO, J. BLUMENSTOCK, AND M. FRASER, *A national plan to enable comprehensive COVID-19 case finding and contact tracing in the US*, tech. rep., Johns Hopkins Bloomberg School of Public Health, Center for Health Security, Baltimore, MD, April 2020.
- [60] Z. WU AND J. M. MCGOOGAN, *Characteristics of and important lessons from the coronavirus disease 2019 (COVID-19) outbreak in China: Summary of a report of 72314 cases from the Chinese Center for Disease Control and Prevention*, *JAMA*, 323 (2020), pp. 1239–1242.
- [61] C. WYMANT, L. FERRETTI, D. TSALLIS, M. CHARALAMBIDES, L. ABELER-DÖRNER, D. BONSALE, R. HINCH, M. KENDALL, L. MILSOM, M. AYRES, C. HOLMES, M. BRIERS, AND C. FRASER, *The epidemiological impact of the NHS COVID-19 app*, *Nature*, (2021).
- [62] W. YANG, S. KANDULA, M. HUYNH, S. K. GREENE, G. VAN WYE, W. LI, H. T. CHAN, E. MCGIBBON, A. YEUNG, D. OLSON, A. FINE, AND J. SHAMAN, *Estimating the infection-fatality risk of SARS-CoV-2 in New York City during the spring 2020 pandemic wave: a model-based analysis*, *Lancet Infect. Dis.*, 21 (2021), pp. 203–212.

APPENDIX: METHODS

SEIHRD Model on a Contact Network

We consider a population of N individuals i (with $i = 1, \dots, N$). At any time t , an individual i is in exactly one of six possible health and vital states:

1. Susceptible $S_i(t)$ when they can get infected with the virus;
2. Exposed $E_i(t)$ when infected with the virus but not yet infectious;
3. Infectious $I_i(t)$ when shedding the virus (with or without clinical symptoms) but not hospitalized;
4. Hospitalized $H_i(t)$ when hospitalized with active disease, in which case individuals are assumed to be shedding the virus;
5. Resistant $R_i(t)$ when immune to the disease through either vaccination or immunity conferred by a prior infection (we assume lifelong resistance for now but can relax that assumption if evidence becomes available that immunity is temporary);
6. Deceased $D_i(t)$.

We take $S_i(t)$, $E_i(t)$, $I_i(t)$, $H_i(t)$, $R_i(t)$, and $D_i(t)$ to be Bernoulli random variables that depend on time t and take only the values 0 and 1. That is, $S_i(t) = 1$ when individual i is susceptible at time t , and otherwise $S_i(t) = 0$ (and analogously for the other variables). Because the six SEIHRD states enumerate all health and vital states of individuals in this model, we have

$$S_i(t) + E_i(t) + I_i(t) + H_i(t) + R_i(t) + D_i(t) = 1. \quad (1)$$

Therefore, there are only 5 independent states.

In the network epidemiology model, a close contact between individuals i and j establishes a temporary network edge with weight $w_{ji}(t) = 1$ for the duration τ of the contact; outside the contact period, $w_{ji}(t) = 0$. Transmission along the temporary edges from one node to another and transitions between health and vital states within each node are modeled as independent Poisson processes [17, 27, 35, 39]. Each process is characterized by a rate that

may vary from node to node and may depend on external variables such as age, sex, and medical risk factors (see Fig. S1 for a schematic).

We make the following assumptions about the transmission rate and the parameters characterizing transition rates between SEIHRD states, including prior distributions used in the network model for DA:

- *Transmission rate:* During the contact period between an infectious or hospitalized individual ($I_j(t) = 1$ or $H_j(t) = 1$) and a susceptible individual ($S_i(t) = 1$), virus can be transmitted across the edge between nodes j and i . When transmission occurs, the susceptible node i becomes exposed and switches state to $E_i(t) = 1$. During the contact period in which an edge is active ($w_{ji}(t) = 1$), we assume the transmission rate to a susceptible node with $S_i(t) = 1$ from an infectious node with $I_j(t) = 1$ is $\kappa_{ji}^I = a_{ji}(t)\beta$, and that from a hospitalized node with $H_j(t) = 1$ is $\kappa_{ji}^H = a'_{ji}(t)\beta$. The parameter β is a transmission rate across active edges, which we set to a global constant in the stochastic surrogate-world simulations and learn on a nodal basis in the model used for DA; $a_{ji}(t)$ and $a'_{ji}(t)$ are time-dependent transmission modifiers that can be adjusted to incorporate additional information that may be available, for example, user-supplied information that individual i is using PPE at time t . In our proof-of-concept simulations, we use $a_{ji}(t) = 0.1$ within hospitals and $a_{ji} = 1$ otherwise. A typical value for the transmission rate of respiratory viruses is around $\beta = 0.5 \text{ h}^{-1} = 12 \text{ day}^{-1}$ [48].

Because we model transmission as a Poisson process, the probability that transmission occurs during contact increases with the duration of the contact period τ , e.g., for an infectious node as [38]

$$T_{ji}(\tau) = 1 - e^{-\kappa_{ji}^I \tau}.$$

(This holds provided the contact period τ is short relative to the duration of infectiousness, so that the infectiousness status of a node does not change during contact.)

In the model used for DA, we do not assume perfect knowledge of the transmission rate; instead, we learn a partial transmission rate β_i for each node i , and compute transmission rates from node j to node i as the averages $\kappa_{ji}^I = 0.5a_{ji}(t)(\beta_i + \beta_j)$ and $\kappa_{ji}^H = 0.5a'_{ji}(t)(\beta_i + \beta_j)$. We assume independent normal priors for β_i for each node, with a mean of 12 day^{-1} and a standard deviation of 3 day^{-1} . We truncate

these distributions to $[1 \text{ day}^{-1}, 20 \text{ day}^{-1}]$, though in practice these bounds are rarely reached.

- *Latent period:* Exposed nodes with $E_i(t) = 1$ transition to being infectious with $I_i(t) = 1$ at the rate σ_i , which is the inverse of the latent period: the time it takes for an exposed individual to become infectious. For COVID-19, the latent period lies between about 2 days and about 12 days [28, 31, 33]. We take the latent period σ_i^{-1} to be fixed for each node i but heterogeneous across nodes. In the model used for DA, we represent it as $\sigma_i^{-1} = 1 \text{ day} + l_i$, where l_i has a gamma prior distribution with shape parameter $k = 1.35$ and scale parameter $\theta = 2 \text{ day}$; hence, the minimum latent period is 1 day, and its prior mean value is 3.7 days ($1 \text{ day} + k\theta$).
- *Duration of infectiousness in community:* Infectious nodes with $I_i(t) = 1$ transition to resistant, hospitalized, or deceased at the rate γ_i , which is the inverse of the duration of infectiousness in the community (i.e., outside hospitals). For COVID-19, the median duration of infectiousness is around 3.5 days [33], but its distribution has a long tail, for example, from individuals with serious or critical disease progression [22]. Like σ_i , we take γ_i to be fixed for each node i but heterogeneous across nodes. In the model used for DA, we model the duration of infectiousness as $\gamma_i^{-1} = 1 \text{ day} + g_i$, where g_i has gamma prior distribution with shape parameter $k = 1.1$ and scale parameter $\theta = 2 \text{ days}$; hence, the minimum duration of infectiousness is 1 day, and its prior mean value is 3.2 days [22, 33].
- *Duration of hospitalization:* Hospitalized nodes with $H_i(t) = 1$ transition to resistant or deceased at the rate γ'_i , which is the inverse of the duration of hospitalization. As before, we take γ'_i to be fixed for each node i but heterogeneous across nodes. In the model used for DA, we model the duration of hospitalization as $\gamma'^{-1}_i = 1 \text{ day} + g'_i$, where g'_i has a gamma prior distribution with shape parameter $k = 1.0$ and scale parameter $\theta = 4 \text{ days}$; hence, the minimum duration of hospitalization is 1 day, and its prior mean value is 5 days. We assume hospitalized nodes are infectious. (If there is evidence that a hospitalized patient no longer sheds the virus, this can be taken into account by setting the transmission rate modifier $a_{ji}(t)$ from the corresponding node to zero; however, we are not considering this situation in our proof-of-concept.)

- *Hospitalization rate*: We assume a fraction h_i of infectious nodes with $I_i(t) = 1$ requires hospitalization after becoming infectious. More precisely, we assume that infectious nodes transition to becoming hospitalized at the rate $h_i\gamma_i$. This implies that, over a period Δt that is short relative to the duration of infectiousness γ_i^{-1} , the probability of transitioning from being infectious to hospitalized, relative to the total probability of leaving the infectious state, is

$$\frac{1 - e^{-h_i\gamma_i\Delta t}}{1 - e^{-\gamma_i\Delta t}} \approx h_i \quad \text{for } \gamma_i\Delta t \ll 1.$$

We take h_i to be fixed for each node i but heterogeneous across nodes; it generally depends on age and other risk factors [7, 60]. We model the age dependence in the stochastic surrogate-world simulations according to clinical data as described below (Table III), and we assume the same parameters in the model used for DA.

- *Mortality rate*: We assume a fraction d_i of infectious nodes with $I_i(t) = 1$ and a fraction d'_i of hospitalized nodes with $H_i(t) = 1$ die. More precisely, we assume infectious nodes die at the rate $d_i\gamma_i$, and hospitalized nodes die at the rate $d'_i\gamma'_i$. Both d_i and d'_i are fixed for each node but are heterogeneous across nodes, depending on age and other risk factors [7, 60]. Both in the stochastic surrogate-world simulation and in the model used for DA, we assume the same age-dependent mortality rates (Table III).
- *Resistance*: For now, we assume resistance to be lifelong, so that an individual who becomes resistant remains so indefinitely and does not return to being susceptible. This assumption can be relaxed by allowing transitions back to the susceptible state if resistance is not permanent.

The health and vital states and transition rates define a Markov chain for the individual-level SEIHRD states. The SEIHRD Markov chain on a contact network can be simulated directly with kinetic Monte Carlo methods [20], as in previous studies [17, 18, 34, 48]. We use kinetic Monte Carlo simulations both to benchmark a model for the SEIHRD probabilities and to provide a surrogate for the real world in our proof-of-concept simulations.

Reduced Master Equations

We are principally interested in the individual SEIHRD probabilities, which are the expected values $\langle S_i(t) \rangle$, $\langle E_i(t) \rangle$, etc. associated with the Bernoulli random variables for the

states. That is, $\langle S_i(t) \rangle$ is the probability that individual i is susceptible at time t .

These probabilities could be obtained as averages over an ensemble of kinetic Monte Carlo simulations; however, it is more computationally efficient to solve reduced master equations for the probabilities directly. The equations are [39, 52]

$$\langle \dot{S}_i \rangle = - [\zeta_i + k_i^x \langle w_i \rangle P(t) \eta_i] \langle S_i \rangle, \quad (2a)$$

$$\langle \dot{E}_i \rangle = [\zeta_i + k_i^x \langle w_i \rangle P(t) \eta_i] \langle S_i \rangle - \sigma_i \langle E_i \rangle, \quad (2b)$$

$$\langle \dot{I}_i \rangle = \sigma_i \langle E_i \rangle - \gamma_i \langle I_i \rangle, \quad (2c)$$

$$\langle \dot{H}_i \rangle = h_i \gamma_i \langle I_i \rangle - \gamma'_i \langle H_i \rangle, \quad (2d)$$

$$\langle \dot{R}_i \rangle = (1 - h_i - d_i) \gamma_i \langle I_i \rangle + (1 - d'_i) \gamma'_i \langle H_i \rangle, \quad (2e)$$

$$\langle \dot{D}_i \rangle = d_i \gamma_i \langle I_i \rangle + d'_i \gamma'_i \langle H_i \rangle, \quad (2f)$$

where

$$\zeta_i(t) = \frac{\sum_{j=1}^N w_{ji}(t) (\kappa_{ji}^I \langle S_i(t) I_j(t) \rangle + \kappa_{ji}^H \langle S_i(t) H_j(t) \rangle)}{\langle S_i \rangle} \quad (2g)$$

is the total infectious pressure on node i from within the network formed by the \tilde{N} users. The infectious pressure represents the possibility of transmission to node i from all network nodes that are at least temporarily connected with node i . Additionally, we have included an exogenous infection rate η_i . This allows for infection from outside the network of \tilde{N} users when the master equation network represents only a subset of a larger network with N nodes, and so transmission can occur from unaccounted nodes. The exogenous infection rate η_i is scaled by the number of external neighbors k_i^x of node i that are not part of the user network, by the probability $\langle w_i \rangle$ of an edge of node i being active, and by the time-dependent prevalence of infectiousness $P(t)$, estimated from the network of \tilde{N} users as described below in (11). Thus, a user surrounded by other users will have no exogenous infection rate, while users with many external neighbors will have a larger exogenous infection rate. The probability of exogenous infection increases with the prevalence of infectiousness within the user base, taken as a proxy of prevalence outside the user base.

We integrate these ordinary differential equations with a Runge-Kutta-Fehlberg 4(5) scheme, with an adaptive timestep of maximum length 3 hours. The weights $w_{ji}(t)$ vary on shorter timescales. This is taken into account in the numerical integration by averaging $w_{ji}(t)$ over the length of a time step, rather than evaluating $w_{ji}(t)$ at discrete intervals.

Closure of Reduced Master Equations

The master equations (2) for the probabilities are not closed because they depend on the joint probabilities $\langle S_i(t)I_j(t) \rangle$ and $\langle S_i(t)H_j(t) \rangle$ in the infectious pressure (Eq. 2g). Various approaches to closing this term have been proposed [27, 39, 52]. Our approach is to estimate it from the ensemble used in the DA cycle, as follows.

The joint-event probability $\langle S_i(t)I_j(t) \rangle$ and the marginal probabilities $\langle S_i(t) \rangle$ and $\langle I_j(t) \rangle$ in the master equations (Eq. 2) are related through the ratio

$$\mathcal{C}[S_i(t), I_j(t)] = \frac{\langle S_i(t)I_j(t) \rangle}{\langle S_i(t) \rangle \langle I_j(t) \rangle}, \quad (3)$$

which is the rescaled joint probability of $S_i(t)$ and $I_j(t)$. We estimate the rescaled joint probability $\mathcal{C}[S_i(t), I_j(t)]$ by its ensemble analogue

$$\mathcal{C}_M[S_i(t), I_j(t)] = \frac{\overline{\langle S_i(t) \rangle \langle I_j(t) \rangle}}{\overline{\langle S_i(t) \rangle} \overline{\langle I_j(t) \rangle}}, \quad (4)$$

where $\overline{(\cdot)} = M^{-1} \sum_m (\cdot)$ denotes the mean over the ensemble (with $m = 1, \dots, M$ labeling ensemble members). Thus, we approximate the joint probability in the infectious pressure (Eq. 2g) as

$$\langle S_i(t)I_j(t) \rangle = \langle S_i(t) \rangle \langle I_j(t) \rangle \mathcal{C}_M[S_i(t), I_j(t)]. \quad (5)$$

With this empirical approximation, we obtain a closed-form expression for the second moment $\langle S_i^m(t)I_j^m(t) \rangle$ for each ensemble member m , which we use in the reduced master equations. The second moment $\langle S_i^m(t)H_j^m(t) \rangle$ follows analogously. If $\mathcal{C}_M[S_i(t), I_j(t)] = 1$ and $\mathcal{C}_M[S_i(t), H_j(t)] = 1$, this reduces to the mean-field approximation that is commonly made in epidemiological models [39, 52] and that often is accurate on real-world networks [21].

We verified this closure against direct kinetic Monte Carlo simulations of the SEIHRD model on the synthetic network described below, in the free-running NYC simulation without lockdown (Fig. 2). The closure has similar performance as the mean-field approximation and adequately, albeit not perfectly, captures the stochastic network dynamics (Figs. S2 and S3). The closure correction coefficients ((4)) concentrate close to the value of 1 (Fig. S4), which explains the similar performance to the mean-field approximation.

Data Assimilation Algorithm

For DA, we use a version of the ensemble adjustment Kalman filter (EAKF) [4], which has previously been used with epidemiological models [33, 41, 42, 51]. EAKF treats an ensemble of M model parameters and states $\langle S_i^m(t) \rangle$, $\langle E_i^m(t) \rangle$, etc. ($m = 1, \dots, M$) from a previous DA cycle as a prior and then linearly updates the ensemble of model parameters and states to obtain an approximate Bayesian posterior given the available data. Unlike other algorithms for computing Bayesian posteriors on networks [3], it makes no assumptions about the network structure, and it scales well to high-dimensional problems [4].

To learn about parameters and the states of nodes on the network, we use a scheme based on iterating forward passes of the master equations over a time window Δ , with EAKF updates between each pass; a similar scheme has been used in epidemiology models before [33, 41, 42, 51]. In this way, we effectively use EAKF as a smoother, harnessing all available data in a DA window $(t_f - \Delta, t_f)$. There are two parts to the DA procedure:

1. Update stage: An EAKF update step is performed to assimilate all data available for the window $(t_f - \Delta, t_f)$, using the previous ensemble model run as prior. The mismatch between the simulated ensemble trajectories and the data is used to update the combined ensemble of parameters and states at the initial time $t_f - \Delta$.
2. Forecast stage: The updated ensemble of states $\langle S_i^m(t_f - \Delta) \rangle$, $\langle E_i^m(t_f - \Delta) \rangle$, etc., with the updated model parameters, is integrated forward up to time t_f , to serve as prior for the next update cycle.

EAKF relies on linear updates and assumes Gaussian error statistics. However, the forward equations (2) are nonlinear. As a result, the EAKF update does not always conserve total probability, in the sense that SEIHRD probabilities for each node will not always sum to 1. We therefore augment the state with an additional total probability conservation variable, with observation equal to the target probability sum 1. The Gaussian assumption is also at odds with probabilities in $[0, 1]$. We have experimented with approaches of transforming variables to an unbounded space, leading to total probability conservation becoming highly nonlinear. We found it to be more robust to work in the original space where total probability conservation is a linear constraint. This approach does, however, violate Gaussianity assumptions about the ensemble when we reinforce the probability bounds by

clipping the states $\langle S_i^m(t_f - \Delta) \rangle$, $\langle E_i^m(t_f - \Delta) \rangle$, etc. to $[0, 1]$.

We assume data errors to be uncorrelated, so that their error covariance matrix is diagonal (see below for how we specify error variances in the proof-of-concept simulations). Prior information on parameters and states is specified in EAKF through the initial condition of the ensemble. We draw the parameters of the ensemble from the above-specified prior distributions, and we initialize the state by seeding each ensemble member with a fraction of (possibly different) infectious nodes, the rest being susceptible. The initial fraction of infectious nodes is drawn from a beta distribution with shape parameters $\alpha = 0.0016$ and $\beta = 1$ (not to be confused with the transmission rate β). The mean fraction (here, 0.16%) of initially infected nodes agrees with the fraction of initially infected nodes in the stochastic surrogate-world simulations.

To account for the multi-fidelity nature of the assimilated data, we perform EAKF in multiple passes. This allows for better conditioned data covariance matrices and for different hyperparameter choices for the different types of data. We perform the following passes to assimilate data from the lowest to the highest fidelity:

- In a first EAKF pass, we update parameters and states at $t_f - \Delta$ using the poorest fidelity data (e.g., temperature sensor data), followed by a forecast over $(t_f - \Delta, t_f)$;
- In a second EAKF pass, we update parameters and states at $t_f - \Delta$ using moderate-accuracy diagnostic test data, followed by another forecast over $(t_f - \Delta, t_f)$;
- In a final EAKF pass, we update parameters and states at $t_f - \Delta$ using data about hospitalization and death status with small error variances, followed by a final forecast over $(t_f - \Delta, t_f)$.

There are three well-established challenges that ensemble-based filters must tackle when assimilating a number of parameters/states that is large relative to the ensemble size [25]: overestimation of long-range covariances, underestimation of variances, and ensemble collapse.

1. To prevent spurious long-range covariances, we localize the effect of observations on states within a single node [5, 25]. That is, direct updates of a nodal state are only due to observations at that node during the DA window. This also provides large

computational savings because EAKF updates may be performed sequentially node-by-node, in any order.

2. To prevent underestimation of variances by the finite-size ensemble, which can lead to discounting of data points [4], and to ensure well-posedness of the matrix inversions, we use regularization of the ensemble covariance matrix Σ . If Λ_{\min} and Λ_{\max} denote the minimum and maximum eigenvalues of Σ , we replace Σ in the EAKF algorithm with $\Sigma + \max(\delta(\Lambda_{\max} - \Lambda_{\min}), \delta_{\min})I$. We choose $\delta = 5/M$ to assimilate diagnostic test data, and $\delta = 1/M$ to assimilate hospitalization/death status; δ_{\min} is taken to be the mean observational noise standard deviation of the update.
3. To prevent ensemble collapse, we add a hybrid inflation to an assimilated state with a map $x \mapsto a(x - \bar{x}) + \bar{x} + N(0, b\bar{x})$, where \bar{x} is the ensemble mean state and $N(0, b\bar{x})$ is Gaussian noise with mean zero and standard deviation $b\bar{x}$ [25]. We take $a = 3.0$ and $b = 0.1$.

Because of the binary nature of the hospitalization and death data, we do not update these states directly; doing so can lead to shocks in the system dynamics. We only update the SEIR states $\langle S_i(t_f - \Delta) \rangle, \langle E_i(t_f - \Delta) \rangle, \langle I_i(t_f - \Delta) \rangle, \langle R_i(t_f - \Delta) \rangle$ at the beginning of a DA window $t_f - \Delta \leq t \leq t_f$ when assimilating hospitalization and death data that fall within the DA window.

Synthetic Network for Proof-of-Concept

We generate a synthetic time-dependent contact network in two steps:

1. We generate a static degree-corrected stochastic block model (SBM) [26, 43], consisting of N nodes in three groups. The three groups represent (a) hospitalized patients, (b) healthcare workers with contacts both within hospitals and in the community, and (c) the community of all remaining individuals (e.g., people in an urban environment). Hospital beds in group (a) are filled when infected nodes become hospitalized; we assume an infinite supply of hospital beds. Healthcare workers in group (b) make up 5% of all nodes, and the remaining 95% of nodes constitute group (c).

We describe connections within groups (a) and (b) with an Erdős–Rényi model and use mean degrees of 5 in group (a) and 10 in group (b), based on a social-contact analyses

in a hospital setting [15]. Hospitalized patients in group (a) can interact only with each other and with the healthcare workers in group (b). To model the interactions between groups (a) and (b), we set the corresponding mean degrees per node to 5 for edges connecting the groups.

We parameterize the contacts among nodes in the community group (c) with a power-law degree correction (corresponding to what is sometimes called a “scale-free” degree distribution) and set the exponent to 2.5, the mean degree to $\hat{k} = 10$, and the maximum degree to 100 [11]; Fig. S5 shows the degree distribution. The community (c) as a group only interacts with healthcare workers (b), and we set the corresponding mean degree to 5.

2. To model time-dependence of the network, we make the edges of the static SBM network created in the first step time-dependent by switching them on and off. That is, neighbors of all nodes remain fixed in time, but their connections are activated or deactivated with time. We account for day/night cycles in the edge weights $w_{ji}(t)$, but we ignore, e.g., weekly cycles. We generate a diurnal cycle that replicates some properties of observed time-dependent human contact networks [54]: The fraction of active edges is small at night and in the early morning hours, reaches a maximum around noon, and approaches small values again in the evening.

To model the time-dependence of $w_{ji}(t)$, we use a birth-death process commonly used in queueing theory. The birth-death process is a Markov chain in which arrivals (edge activations) are inhomogeneous Poisson processes with a diurnally varying mean rate $A_{ji}(t)$; contact durations are exponentially distributed with a mean contact duration τ (i.e., a mean rate parameter $\mu = \tau^{-1}$). We choose a mean duration of $\tau = 2$ min (hence $\mu = 720 \text{ day}^{-1}$), based on high-resolution human contact data [48]. We model the mean edge activation rate as

$$A_{ji}(t) = \frac{1}{\hat{k}} \max \left\{ \min(\lambda_{j,\min}, \lambda_{i,\min}), \min(\lambda_{j,\max}, \lambda_{i,\max}) \left[1 - \cos^4 \left(\frac{\pi t}{1 \text{ day}} \right) \right]^4 \right\}. \quad (6)$$

Here, $t = 0$ starts at midnight, and \hat{k} is the mean degree of the network in the community group (c), so that $\hat{k}A_{ji}$, when averaged over edges, is an average contact rate per node. The diurnally averaged edge activation rate then is

$$\bar{A}_{ji} = \frac{1}{1 \text{ day}} \int_0^{1 \text{ day}} A_{ji}(t) dt. \quad (7)$$

For the minimum and maximum contact rates per node, $\lambda_{i,\min}$ and $\lambda_{i,\max}$, we choose the default values $\lambda_{\min} = 4 \text{ day}^{-1}$ and $\lambda_{\max} = 84 \text{ day}^{-1}$. If the default contact rates apply for all nodes, this gives for the community group (c) a mean contact rate per node of

$$\hat{k}\bar{A}_{ji} \approx 37.7 \text{ day}^{-1}; \quad (8)$$

this is about a factor 3–4 larger than typical human contact rates as assessed by self-reports [36], consistent with the fact that we also take fleeting contacts into account that would likely not be self-reported. The minimum and maximum contact rates $\lambda_{i,\min}$ and $\lambda_{i,\max}$ for a node i are the principal parameters we vary to explore the effect of contact interventions. Reducing $\lambda_{i,\min}$ and $\lambda_{i,\max}$ for a node reduces the fraction of time edges connecting to node i are active.

The time dependencies of all edges $w_{ji}(t)$ are treated as independent. We update the time-dependence of each edge at midnight every simulated day, running independent birth-death processes with parameters $A_{ji}(t)$ and μ for the next day.

If a node becomes hospitalized, it is deactivated at its previous location in the network and transferred to the hospital group (a). Hospitalized nodes are assumed to be infectious. (This assumption may later be relaxed to model the situation that a patient is no longer infectious but may still be hospitalized with ongoing disease.)

Selection of Subnetwork for User Base

To select a subnetwork for a user base with $\tilde{N} < N$ users, we construct subgraphs with two different topologies. First, a neighbor-based subgraph is constructed from a randomly selected seed user, by adding all neighbors of this user to the subgraph, then in a greedy fashion adding all neighbors of each member of this new subgraph, and so on, until a desired user population is reached. Second, a random subgraph is constructed by randomly choosing nodes from the full network. Figure S6 illustrates the different user base topologies, and Table I summarizes their characteristics.

Type	Population	Interior	Exterior connectivity
75% neighbor	73,456	21,499	1.9
50% neighbor	48,971	6,301	5.2
25% neighbor	22,381	2,107	10.0
75% random	73,353	7,061	3.1
50% random	48,371	550	6.3
25% random	24,482	33	9.3

TABLE I. Details of the different user bases. The percentage represents approximately \tilde{N}/N , for the user population \tilde{N} . The interior defines how many users are completely surrounded by other users. The exterior connectivity gives the average number of exterior nodes connected to a node inside the user base.

Surrogate World Simulation

To generate surrogate worlds with which to test the DA algorithm and interventions, we simulate epidemics on the synthetic network stochastically with kinetic Monte Carlo methods [20]. For these stochastic simulations (but not for the model used for DA), we choose mean transmission and transition rates between SEIHRD states that are homogeneous across nodes, except for hospitalization and mortality rates that depend on age. The mean rates we use are based on current knowledge about COVID-19 (Table II). We simulate 20 epidemics that only differ in their random seed. They are initialized on March 5, 2020, with 0.16% of nodes randomly assigned to be infectious.

The dependencies of the hospitalization rate $h_i = h(a)$ and mortality rates $d_i = d(a)$ and $d'_i = d'(a)$ on age a are estimates based on recent data (Table III).

To model age-dependent disease progression, we randomly assign ages to network nodes in the community group (c) according to the age distribution for NYC, as given by U.S. Census data [55]. Assumptions about the age dependence of disease progression and other model parameters are immaterial for the risk assessment platform—the platform can learn such parameters and parametric functions from data; we merely use them to create a reasonably realistic surrogate of the real world. We assign ages to nodes in the healthcare worker group (b) according to the age distribution among working-age adults (21–65 years old). Initially,

Parameter	Value
β, κ^I	12 day ⁻¹
κ^H	0.1 β
σ	(3.7 day) ⁻¹
γ	(3.2 day) ⁻¹
γ'	(5 day) ⁻¹
λ_{\max}	84 day ⁻¹
λ_{\min}	4 day ⁻¹

TABLE II. Mean transmission and transition rates and maximum/minimum contact rates for the surrogate-world simulations with the stochastic SEIHRD model (Fig. S1). The mean rates are taken to be the same for all nodes; hence, the nodal indices are suppressed. The latent period σ^{-1} and duration of infectiousness in the community γ^{-1} are approximated from those in refs. [33] and [22]; the duration of hospitalization γ'^{-1} is from ref. [46], and the transmission rate β is fit to be consistent with data for respiratory viruses [48] and to roughly reproduce NYC data.

there are no hospitalized nodes (i.e., group (a) is empty).

The network has 97,942 nodes. We choose the global mean transmission rate β so that our simulations are qualitatively aligned with the evolution of the COVID-19 epidemic in NYC [1]. We find that a global value of $\beta = 12 \text{ day}^{-1}$ can qualitatively reproduce the observed rate of infections and can quantitatively reproduce the rate of hospitalizations and deaths during the initial phases of the epidemic in NYC.

Synthetic Data

We sample synthetic data from the stochastic surrogate-world simulation on the network with N nodes and assimilate data for a possible subset of $\tilde{N} \leq N$ users in the reduced master equation model. We consider the following data and error rates:

- A positive virus test for node i is taken to imply

$$\langle I_i(t) \rangle = \text{PPV} \tag{9}$$

at the time the test sample is taken. The positive predictive value (PPV) is calculated

Age group a (yrs)	$f(a)$	$h(a)$	$d(a)$	$d'(a)$
0–17	20.7%	0.2%	0.0001%	1.9%
18–44	40.0%	1.0%	0.001%	7.3%
45–64	24.5%	4.0%	0.1%	19.3%
65–74	8.3%	7.6%	0.7%	32.7%
≥ 75	6.5%	16.0%	1.5%	51.2%

TABLE III. Age-dependent mean hospitalization and mortality rates in the surrogate-world simulation. The share $f(a)$ of the population in each age group a is taken from U.S. Census data [55]. The age-dependent death rate in hospitals d' is obtained from cumulative hospitalization and death rates in NYC by June 1, 2020 [1], under the assumption that 90% of deaths occurred in hospitals. Age-dependent hospitalization rates $h(a)$ and mortality rates $d(a)$ in the community (outside hospitals) are difficult to obtain directly from NYC data because of an age-dependent undercount of infections [62]. We choose hospitalization rates $h(a)$ that approximate data from France [49], adjusting the rates so that the overall hospitalization rate is $\sum_a f(a)h(a) \approx 3.1\%$, which is NYC’s overall hospitalization rate if one assumes a cumulative COVID-19 incidence rate of 23% [47], together with NYC’s actual hospitalization count (52,333 on June 1, 2020) and population (8.34 million) [1]. Similarly, the mortality rate in the community $d(a)$ is chosen such that the overall infection fatality rate is $\sum_a f(a)[d(a) + h(a)d'(a)] \approx 1.1\%$, which is NYC’s overall infection fatality rate if one considers the same cumulative incidence of 23% and the confirmed and probable cumulative death count from COVID-19 (21,607 by June 1, 2020).

as

$$\text{PPV} = \frac{\text{sensitivity} \times P(t)}{\text{sensitivity} \times P(t) + (1 - \text{specificity}) \times (1 - P(t))}, \quad (10)$$

where we take the sensitivity of the test to be 80% and the specificity to be 99%, which we use as an approximation of the currently imprecisely known actual sensitivities and specificities [50, 58]. As an estimate of the infectiousness prevalence $P(t)$ in the population, we use the average of the infectiousness probabilities both over the network of size \tilde{N} and over the ensemble of size M ,

$$P(t) = \max \left(\frac{1}{\tilde{N}M} \sum_{m=1}^M \sum_{i=1}^{\tilde{N}} \langle I_i^m(t) \rangle, \frac{1}{\tilde{N}} \right). \quad (11)$$

The cutoff of \tilde{N}^{-1} is included to guard against erroneously assuming prevalence to be zero because of subsampling on the reduced network. For the DA, we assume an error rate of $1 - \text{PPV}$ for a positive test result.

- A negative virus test for node i is similarly taken to imply

$$\langle I_i(t) \rangle = \text{FOR} \tag{12}$$

at the time the test sample is taken. The false omission rate (FOR) is calculated as

$$\text{FOR} = \frac{(1 - \text{sensitivity}) \times P(t)}{(1 - \text{sensitivity}) \times P(t) + \text{specificity} \times (1 - P(t))},$$

with the same sensitivity, specificity, and prevalence as for a positive virus test. For the DA, we assume an error rate equal to FOR for a negative test result.

- To assimilate low-fidelity data such as those from temperature sensors, we assume $\langle I_i(t) \rangle = \text{PPV}$ as for a positive virus test when they indicate infectiousness (e.g., when a temperature reading is elevated). However, we use a sensitivity of 20% and specificity of 98% to reflect the lack of sensitivity of temperature sensors in detecting COVID-19 infection [10]. For the DA, we assume an error rate equal to $1 - \text{PPV}$, analogous to a positive virus test.
- Data about hospitalization with COVID-19 imply that $H_i(t) = 1$ for the duration of hospitalization. We assume the hospitalization status of all users to be known with certainty, that is, we assimilate the hospitalization status $H_i(t) = 0$ or $H_i(t) = 1$ for all users; however, we only update the SEIR probabilities at the beginning of a DA window $t_f - \Delta \leq t \leq t_f$ with hospitalization data.
- Death implies $D_i(t) = 1$. We assume the vital status of all users to be known with certainty, that is, we assimilate $D_i(t) = 0$ or $D_i(t) = 1$ for all users; as for hospitalization, however, we only update the SEIR probabilities at the beginning of a DA window $t_f - \Delta \leq t \leq t_f$ with death data.
- For completeness, we state that a positive serological test for SARS-CoV-2 for node i would be taken to imply

$$\langle R_i(t) \rangle = \text{PPV},$$

with the positive predictive value calculated from (10). Typical values for sensitivity would be 90% and for specificity 95% [56], and the prevalence of resistance can be estimated from the resistance probabilities on the reduced master equation network. We would again assume an error rate equal to $1 - \text{PPV}$. However, we did not assimilate simulated serological tests in our proof-of-concept because currently achievable serological test rates are low.

To model data errors, we randomly corrupt the synthetic data sampled from the surrogate world network with the false positive and false negative rates implied by the sensitivity (false negative rate = $1 - \text{sensitivity}$) and specificity (false positive rate = $1 - \text{specificity}$).

Testing Strategy

Because of the low prevalence of disease, we use a simple testing strategy that randomly tests a given budget of nodes once per day. It is possible that more intelligent targeting strategies for tests, based on the estimated nodal states and the network structure, would be more effective in finding new cases. Our framework can provide a testbed for developing such strategies.

Parameter Learning In addition to assimilating probabilities of SEIHRD states, we can in principle learn about parameters in the reduced master equation model (2), for example:

- Individual partial and time-dependent transmission rates β_i ;
- Individual inverse latent periods σ_i ;
- Individual inverse durations of infectiousness γ_i and hospitalization γ'_i ;
- Individual hospitalization rates h_i and mortality rates d_i and d'_i ;
- Exogenous infection rates η_i .

We have not fully explored the efficacy of learning about all these different parameters from data. For now, we include only the partial transmission rates β_i , the inverse latent periods σ_i , and the durations of infectiousness γ_i and hospitalization γ'_i in the DA, all with the priors stated above. Figure S12 shows the prior distributions of the parameters at the beginning of the epidemic. and the posterior distributions as the epidemic evolves and the network

model learns about the parameters. The results show that the DA does not refine the prior estimates of the parameters.

The hospitalization rates h_i and mortality rates d_i and d'_i are fixed at the same values as in the stochastic surrogate-world simulation (Table III). We assume the exogenous infection rates η_i to be equal to the partial transmission rates β_i , and we estimate the probability of an edge of node i being active as

$$\langle w_i \rangle = \frac{\bar{A}_i}{\mu + \bar{A}_i}, \quad (13)$$

where \bar{A}_i is the diurnally averaged edge activation rate,

$$\bar{A}_i = \frac{1}{1 \text{ day}} \int_0^{1 \text{ day}} A_i(t) dt, \quad (14)$$

with

$$A_i(t) = \frac{1}{\hat{k}} \max \left\{ \lambda_{i,\min}, \lambda_{i,\max} \left[1 - \cos^4 \left(\frac{\pi t}{1 \text{ day}} \right) \right]^4 \right\}. \quad (15)$$

With our parameters, this is $\bar{A}_i = \lambda_{i,\min}/\hat{k} = 0.4 \text{ day}^{-1}$ for isolated nodes and $\bar{A}_i = 3.77 \text{ day}^{-1}$ otherwise. For a stationary birth-death process, this estimate for $\langle w_i \rangle$ is the stationary probability of an edge being active; it approximates the diurnally averaged probability in the case of the birth-death process with diurnally varying edge activation rates. Through this probability $\langle w_i \rangle$, the exogenous infectious pressure depends on the isolation status of a node.

Classification of Disease Status Nodes i in the community group (c) are classified as possibly infectious ($\mathcal{I}_i = 1$) or not ($\mathcal{I}_i = 0$) according to

$$\mathcal{I}_i = \begin{cases} 1 & \text{if } \overline{\langle I_i^m \rangle} > c_I, \\ 0 & \text{otherwise.} \end{cases} \quad (16)$$

Here, c_I is a classification threshold, which can be determined from receiver operating characteristic (ROC) curves as some optimum tradeoff between wanting to achieve high true positive rates while keeping false positive rates modest. The ROC curves we use are adapted to the setting in which we are primarily interested in the fraction of users that is classified as possibly infectious (and thus may be asked to self-isolate). We plot the true positive rate (TPR, nodes with $\mathcal{I}_i = 1$ for which $I_i = 1$ in the stochastic simulation) against the predicted positive fraction (PPF, fraction of nodes with $\mathcal{I}_i = 1$ in the user base of size \tilde{N}). ROC curves are traced out by lowering the classification threshold c_I , thereby increasing both TPR and PPF.

Contact Interventions We implement two types of intervention scenarios in our test cases. In the first, a lockdown scenario (Fig. 2), we set $\lambda_{i,\max}$ for all nodes in the community group (c) to 33 day^{-1} . This amounts to a reduction of the mean contact rate ((8)) in group (c) by 58%. In the second, a time-limited isolation intervention, we reduce the contact rates of targeted high-risk nodes by setting $\lambda_{i,\max} = \lambda_{i,\min} = 4 \text{ day}^{-1}$; thus, these high-risk nodes are assumed to self-isolate, with only 4 contacts per day on average, corresponding to a reduction of their average contact rate by 91%.

The duration of contact reduction takes three possible values. In the lockdown scenario (Fig. 2), all nodes have contact reduction from the inception of the lockdown until the end of the simulation. In the TTI scenario, self-isolating nodes have contact reduction for 14 days, in accordance with current CDC guidelines [13], after which contact rates are reset to the original values. For the network DA scenario, self-isolating nodes have contact reduction until they are classified as negative ($\langle \overline{I_i^m} \rangle \leq c_I$) for a period of 5 consecutive days, after which contact rates are reset to their original values. This corresponds to reinstatement of original contact rates for 50%, 90% and >99% of isolated nodes within 7, 14 and 21 days, respectively.

SUPPLEMENTARY FIGURES

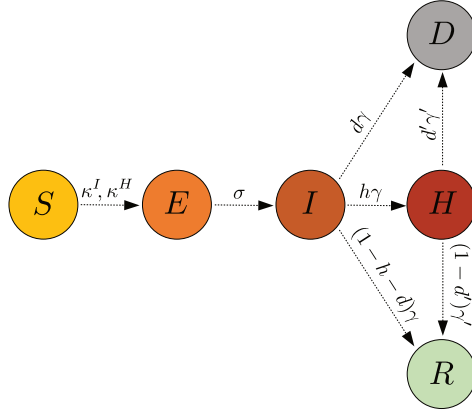


FIG. S1. Schematic of SEIHRD model [7]. Infected and hospitalized nodes infect susceptible nodes at rates κ^I and κ^H , respectively. After being infected, susceptible nodes become exposed. Exposed nodes become infectious at rate σ . Infected nodes may get hospitalized at rate $h\gamma$, die at rate $d\gamma$, or become resistant at rate $(1-h-d)\gamma$. Once hospitalized, nodes either become resistant at rate $(1-d')\gamma'$ or die at rate $d'\gamma'$.

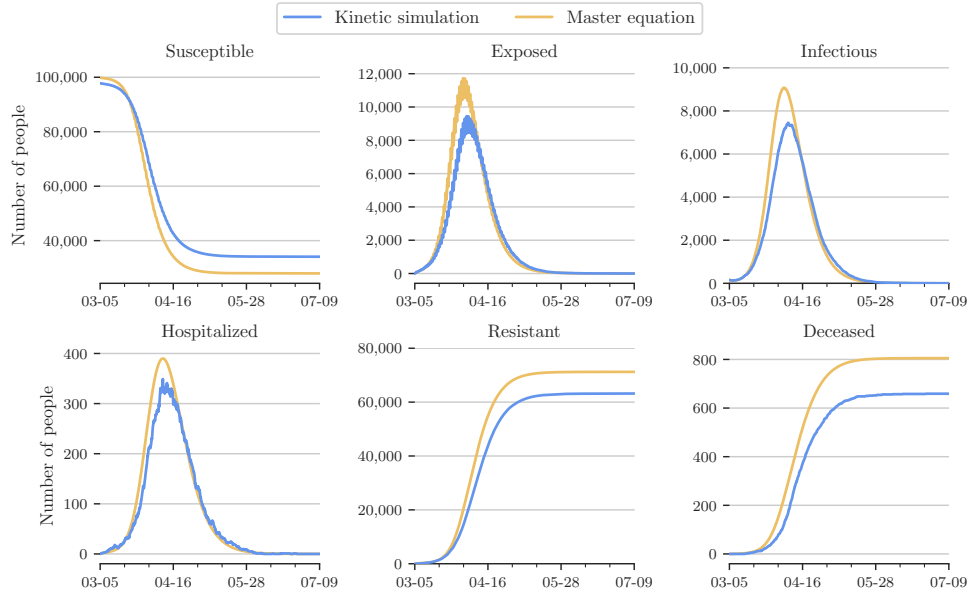


FIG. S2. Overall epidemic dynamics from SEIHRD model using mean-field approximation.

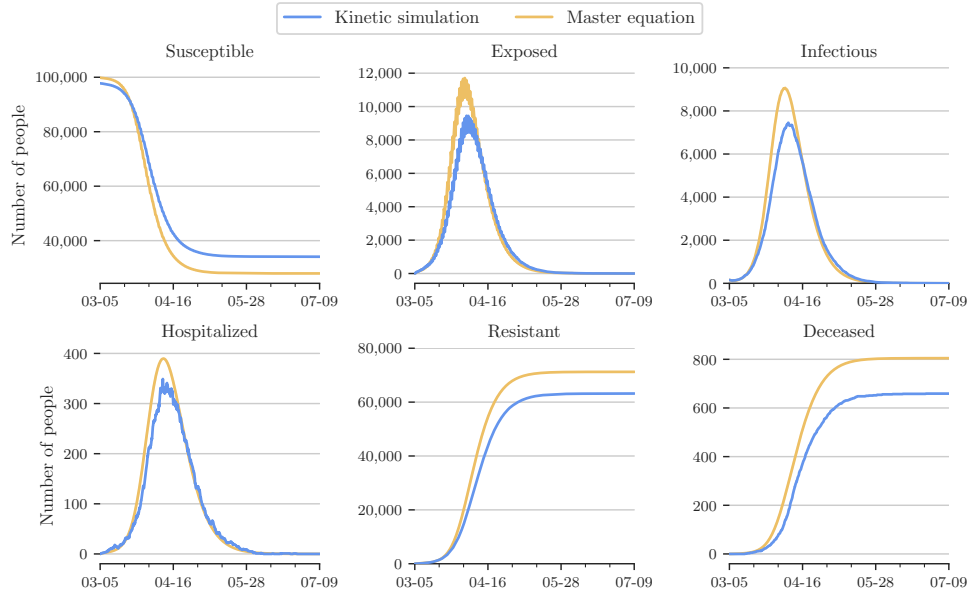


FIG. S3. Overall epidemic dynamics from SEIHRD model using mean-field approximation with ensemble correction.

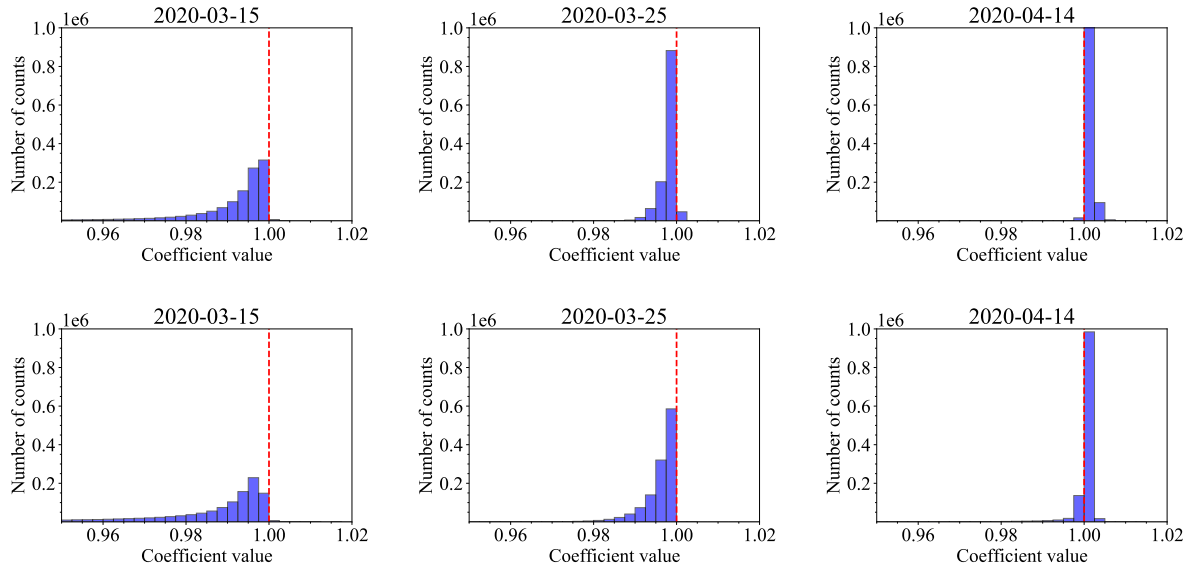


FIG. S4. Histograms of correction coefficients (top row) $\mathcal{C}_M[S_i(t), I_j(t)]$ and (bottom row) $\mathcal{C}_M[S_i(t), H_j(t)]$ at different times during the simulated epidemic.

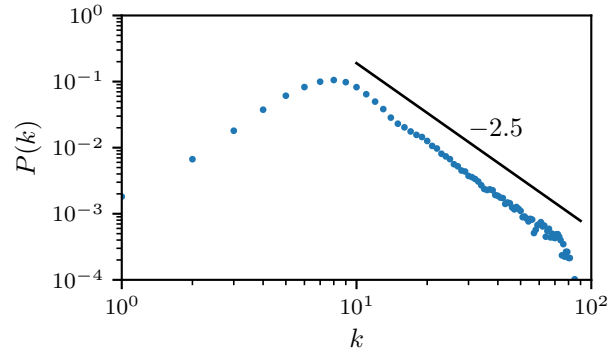


FIG. S5. Distribution of degrees k in synthetic contact network with 97,942 nodes.

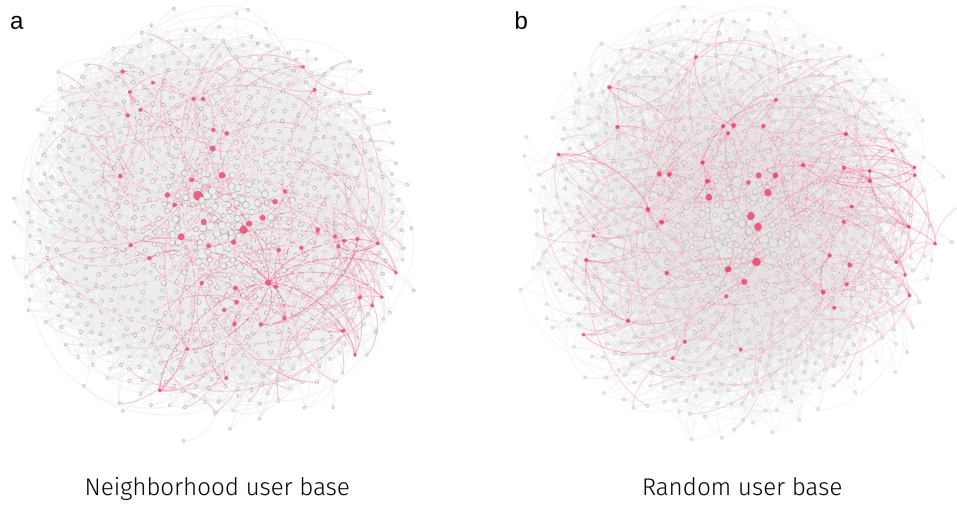


FIG. S6. Illustration of different user base topologies. (a) Neighbor-based user base, constructed by iteratively adding neighborhoods. (b) Random subnetwork of users. Red nodes and edges are part of a user base, grey nodes and edges of the overall population. The shown networks have 982 nodes and 5,916 edges. Both user bases contain 5% of all nodes.

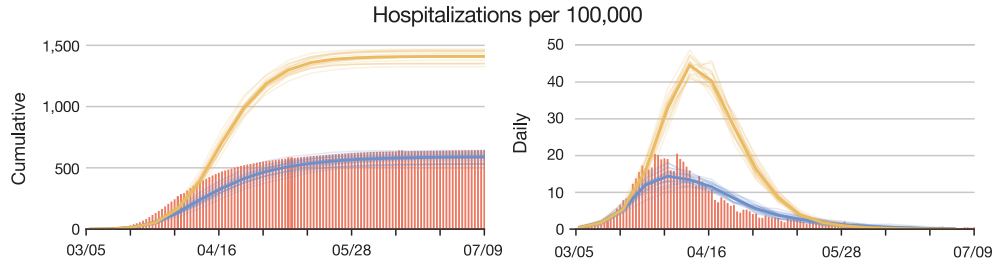


FIG. S7. Hospitalization rates in surrogate-world simulation with a lockdown (blue) and without (orange). The left panel shows cumulative hospitalizations and the right panel daily hospitalizations per 100,000 population for the same simulations as those in Fig. 2. Red bars represent COVID-19-related hospitalization rates for New York City [1]. As in Fig. 2, the simulation data are smoothed with a 7-day moving average filter.

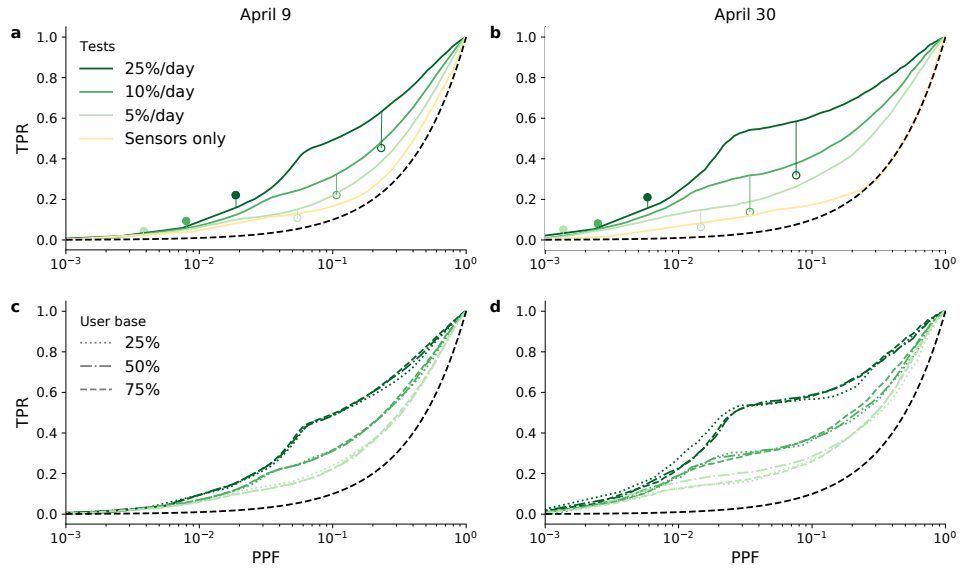


FIG. S8. Receiver operating characteristic (ROC) curves for classification as possibly infectious. As in Fig 3, but for subnetworks with randomly selected nodes rather than for subnetworks with a neighborhood topology.

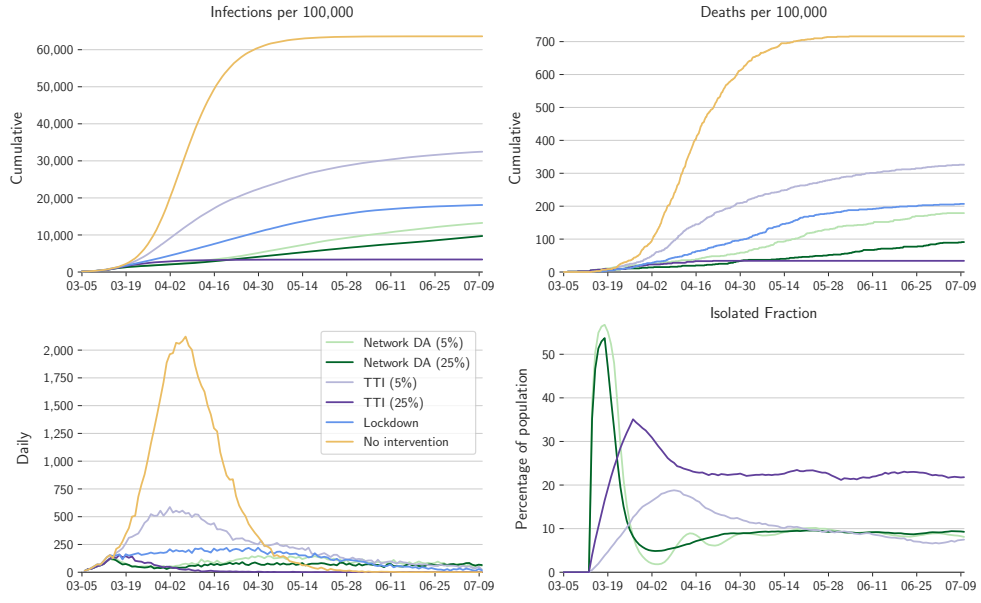


FIG. S9. Comparison of different contact intervention scenarios for random user base with $\tilde{N}/N = 75\%$. As in Fig. 5, but with a subnetwork with randomly selected nodes and with a classification threshold $c_I = 0.25\%$.

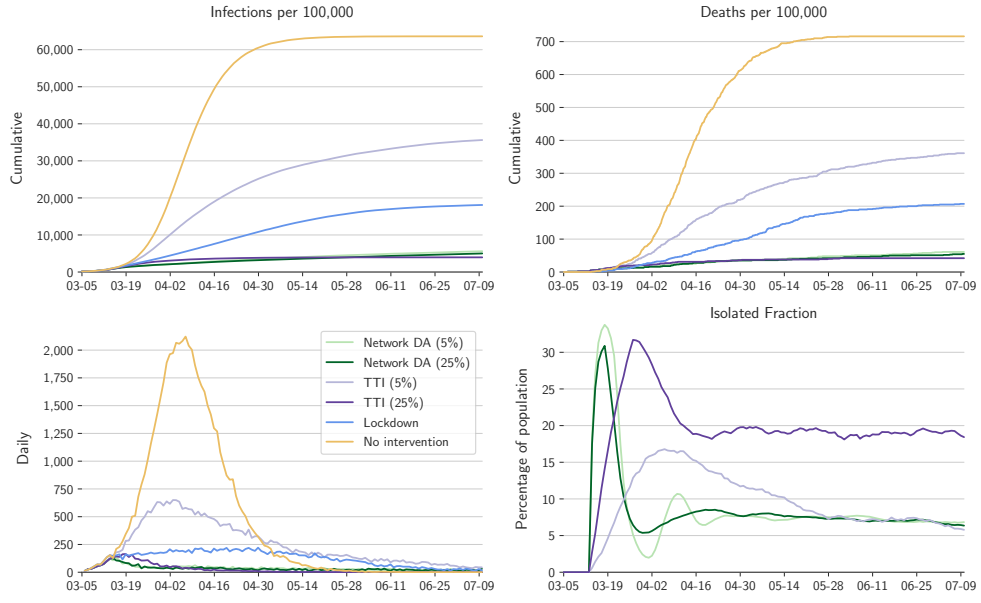


FIG. S10. Comparison of different contact intervention scenarios for neighborhood user base with $\tilde{N}/N = 50\%$ and with a classification threshold $c_I = 0.5\%$.

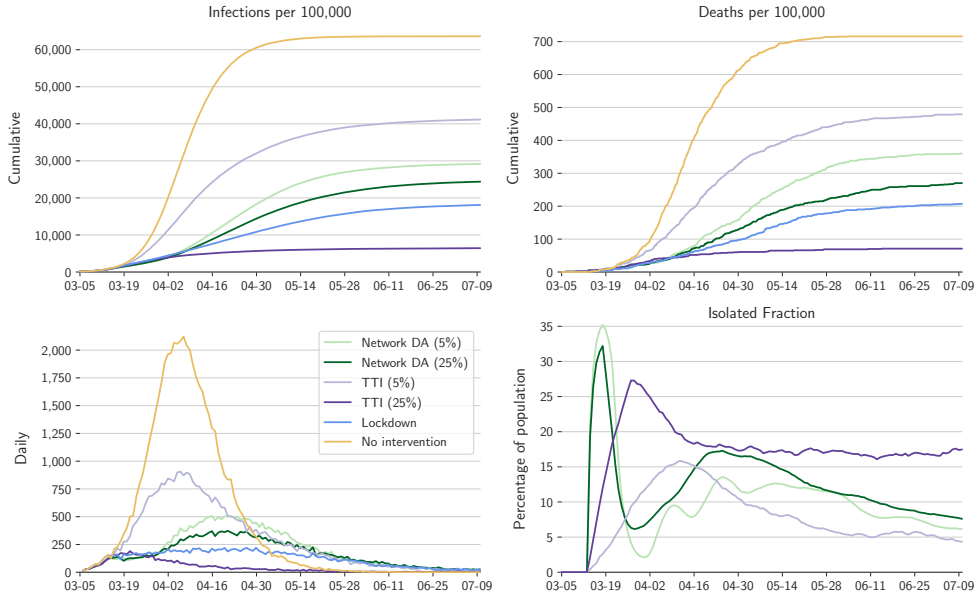


FIG. S11. Comparison of different contact intervention scenarios for random user base with $\tilde{N}/N = 50\%$ and with a lower classification threshold $c_I = 0.25\%$. As in Fig. S10, but with a subnetwork with randomly selected nodes.

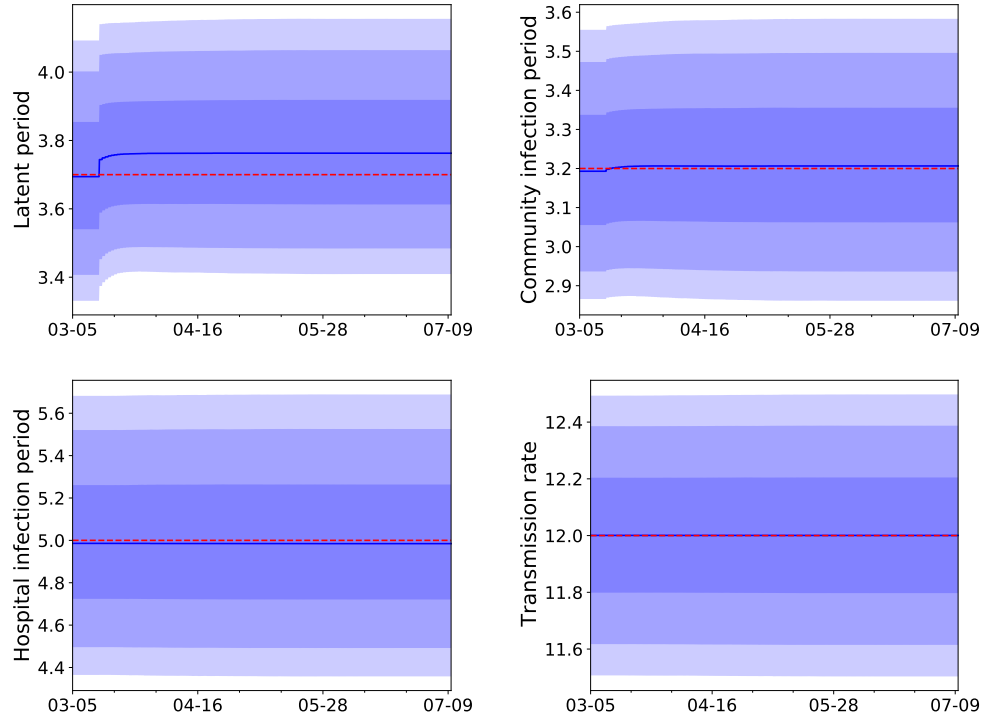


FIG. S12. Distribution of ensemble averaged model parameters across nodes as a function of time during the epidemic. The shaded regions contain 50%, 80% and 90% of the distribution. The dashed line represents the true parameters in the stochastic simulation. During the first 8 days, no DA is performed, and the parameter distributions are the prior distributions.